Mathematics

https://www.aimspress.com/journal/Math

AIMS Mathematics, 11(8): 25526–25552.
DOI:10.3934/math.20261024
Received: 23 June 2026
Revised: 28 July 2026
Accepted: 11 August 2026
Published: 18 August 2026

Research article

Bifocusing method for localizing small objects with an incomplete multi-static response matrix from transverse electric polarized waves

Taeyoung Ha[1,†], Sangwoo Kang[2,†], Minyeob Lee[3,†], Won-Kwang Park[3,†,*], and Seong-Ho Son[4,5,†]

[1] Division of Industrial Mathematics, National Institute for Mathematical Sciences, Daejeon 34047, Korea

[2] Graduate School of Data Science, Pusan National University, Pusan 46241, Korea

[3] Department of Mathematics, Kookmin University, Seoul 02707, Korea

[4] Department of ICT Convergence, Soonchunhyang University, Asan 31538, Korea

[5] Department of Mechanical Engineering, Soonchunhyang University, Asan 31538, Korea

* **Correspondence:** Email: parkwk@kookmin.ac.kr.

Abstract: This work investigated the application of the bifocusing method (BFM) in inverse scattering problems to detect small objects using transverse electric polarized waves. In practical experimental setups, restrictions on the scanning trajectory of receivers often lead to an incomplete multi-static response (MSR) matrix. Moreover, the direct application of the standard BFM imaging function-designed based on the structure of the measured scattered field-is mathematically problematic since its denominator can become zero at specific evaluation points. To overcome these limitations, we proposed a modified BFM-based imaging function and derived an asymptotic representation as an infinite series comprising Bessel functions of the first kind, the objects' material properties, and the receivers' angular aperture. This result elucidates the dependency of the imaging results on the sizes and permeabilities of the targets, and provides a logical basis for the frequency-dependent trade-off between image resolution and artifact generation. The validity of the theoretical result was corroborated through numerical simulations using noise-corrupted synthetic data for objects with diverse sizes and material properties, as well as a 2D Fresnel experimental dataset.

Keywords: bifocusing method; inverse scattering problems; transverse electric polarization; Bessel functions; multi-static response matrix; small-object detection; imaging functional
Mathematics Subject Classification: 78A46

[†]These authors contributed equally to this work and share first authorship.

1. Introduction

The primary objective of inverse scattering problems is to retrieve the physical properties—such as the location, shape, and material characteristics—of unknown objects from measured scattered fields [1–3]. Due to their fundamental nonlinearity and severe ill-posedness, these problems are notoriously difficult to solve. Nevertheless, given their profound significance across various disciplines—including mathematics, engineering, medicine, and physics—researchers have developed a wide array of algorithms, predominantly based on Newton-type iterative schemes.

Among iterative approaches, gradient-based and Newton-type schemes have been widely investigated. Notable examples include a focusing-based iterative Newton technique for retrieving the electrical profile of a nonmagnetic object [4], a regularized Newton-type iteration scheme for reconstructing an open sound-hard crack using phaseless far- and near-field data [5], the contrast source inversion (CSI) approach for retrieving a heterogeneous dielectric profile in the ablation zone [6], a partial differential equation (PDE)-constrained optimization method for reconstructing the dielectric properties of a medium in microwave imaging [7], an optimal control technique for shape reconstruction of 2D extended scatterers [8], and a surrogate-model-free iterative method for retrieving 3D objects [9]. Alongside these deterministic methods, other distinct methodologies have been developed, such as the magnetic resonance electrical impedance tomography (MREIT) technique for visualizing conductivity images of an electrically conducting object [10] and a numerical convexification algorithm for the simultaneous reconstruction of dielectric permittivity and electric conductivity [11]. Furthermore, stochastic and global optimization techniques, including a particle swarm optimization (PSO) algorithm for 3D medical image registration [12] and a modified two-step Monte Carlo continuation algorithm for the inverse scattering problem of acoustic-elastic interaction with random periodic interfaces [13], have been utilized to explore the solution space.

While these diverse iterative approaches can yield highly accurate reconstructions, they each face specific methodological challenges. Traditional Newton-type and gradient-based methods are highly susceptible to converging to local minima, require complex selection of appropriate regularization schemes, and often face non-convergence issues. Consequently, their successful application relies heavily on a highly reliable initial guess [14, 15]. Conversely, global optimization methods like PSO and Monte Carlo approaches mitigate the initial guess dependence but typically demand exceptionally high computational costs. Motivated by these respective limitations, various non-iterative algorithms have been actively developed to efficiently identify the location or shape of unknown scatterers without any prior information. For example, these include the direct sampling method [16–18], factorization method [19–21], migration techniques [22–24], MUltiple SIgnal Classification (MUSIC) algorithm [25–27], linear sampling method [28–30], orthogonality sampling method [31–33], and topological derivative-based methods [34–36].

Among these qualitative approaches, the bifocusing method (BFM) has proven to be a valuable imaging technique utilizing a multistatic measurement system in both inverse scattering problems and microwave imaging. Notable applications include damage detection in concrete voids [37], ultra-wide-band tomographic radar imaging [38, 39], anomaly detection from scattering parameter data [40–42], and the real-time tracking of moving small objects without incident field data [43]. Recently, the mathematical structure of the BFM-based imaging function has been revealed under the assumption that complete elements of the so-called multi-static response (MSR) matrix are collected;

its applicability has also been theoretically explored in [44].

Despite its theoretical appeal, deploying the BFM in real-world scenarios introduces significant physical and mathematical hurdles. In practical experimental setups, such as the 2D Fresnel experimental configuration, there are inherent restrictions on the scanning trajectory of receivers. For a given transmitter position, an active receiver typically only covers a partial angular sector. These physical constraints prevent the acquisition of full measurement data, which often leads to an incomplete MSR matrix. Although constructing a full MSR matrix is practically unachievable, it remains possible to retrieve small objects using the standard BFM-based imaging function for transverse magnetic (TM) polarized waves, and the theoretical basis for its applicability was established in [45]. As indicated above, most research has focused on applying the BFM to TM polarization. To the best of our knowledge, there exist very few theoretical studies regarding BFM-based imaging for transverse electric (TE) polarized waves.

In this paper, we consider the application of the BFM for identifying the existence, location, and shape of small objects in limited-aperture inverse scattering problems using TE polarized waves. It is important to emphasize that the direct application of the standard BFM-based imaging function is mathematically problematic. Because the traditional function evaluates the synthesis inversion of the gradients of Green's functions, it carries the inherent risk that its denominator can become zero at specific evaluation points within the domain [44]. This fundamental flaw can lead to unexpected blow-ups and severe instability in the imaging results, making the conventional formulation inappropriate for retrieving target objects. For this reason, a modified BFM-based imaging function is proposed to overcome these practical limitations and mathematical instabilities. To bypass the mathematical risk of a zero denominator, the proposed approach avoids unexpected blow-ups by replacing the inner product of the gradients of Green's functions with the product of Green's functions themselves. Moreover, to address the issue of incomplete data, we partition the receiver indices and construct an adapted MSR matrix by assigning a value of zero to the unmeasured scattered field data, motivated by several studies [30, 35, 46]. Within the framework of the BFM approach, setting these unmeasured values to zero is well-justified. As demonstrated in recent literature on microwave imaging [42], this specific zero-padding strategy within the BFM guarantees the best localization results for small objects.

In addition to demonstrating the applicability of the designed imaging function, we rigorously prove that the imaging function can be represented as an infinite series comprising Bessel functions of the first kind, the objects' material properties, and the receivers' angular aperture. This result elucidates the strong dependency of the imaging results on both the sizes and the magnetic permeabilities of the targeted objects, providing a logical, theoretical basis for the frequency-dependent trade-off observed in microwave imaging: the balance between achieving high image resolution at sufficiently high frequencies and the generation of unwanted artifacts. In order to validate the theoretical result, various numerical simulation results using noise-corrupted synthetic data are presented. Additionally, the applicability of the methodology is validated against a 2D Fresnel experimental dataset [47], specifically targeting the identification of a perfectly conducting metallic object characterized by a non-smooth Lipschitz boundary.

To explicitly clarify the novelty of this study relative to the existing literature, the key differences between the present work and the recent study [44] are summarized as follows: First, the theoretical and numerical results in [44] rely on the ideal assumption that all elements of the MSR matrix are completely measurable. In contrast, our current work explicitly deals with practical, real-world situations where the MSR matrix is inherently incomplete due to limited-aperture constraints. Second, although [44] noted the potential applicability of the BFM to limited-aperture problems using an experimental Fresnel dataset, it explicitly designated the theoretical investigation of this topic as a significant future research endeavor. The present study actively bridges this gap by establishing a rigorous theoretical framework for the BFM under limited-aperture inverse scattering configurations utilizing transverse electric (TE) polarized waves. Therefore, the primary novelty of our work is not Green-function-based denominator modification itself—which is an existing remedy—but rather the first successful application and theoretical justification of this modified functional under practical, incomplete multi-static response (MSR) conditions. Finally, under the ideal full MSR conditions described in [44], the TE polarization imaging functional inherently produces a ring-like shape at the actual location of the object, which complicates precise localization. However, in the limited-aperture problems addressed in this study, we demonstrate that the BFM-based imaging functional effectively eliminates this ring artifact. Instead, it generates a distinct, large peak exactly at the object's location, allowing for highly accurate positional recognition. Consequently, we elucidate the reasoning behind this phenomenon and demonstrate that the proposed functional provides reliable qualitative localization of the target objects.

This paper is organized as follows. In Section 2, the fundamental concepts of the 2D forward problem, data measurement configuration, representation formula for the scattered field, and the modified BFM-based imaging function are presented. In Section 3, we analyze the mathematical structure of the imaging function and discuss the applicability of object identification, the dependence on material properties, and qualitative localization. In Section 4, various numerical simulation results using synthetic datasets corrupted by random noise and a 2D Fresnel experimental dataset are exhibited to support the theoretical findings. A short conclusion including future perspectives is provided in Section 5.

2. Traditional and modified imaging functions for the bifocusing method

2.1. Problem formulation, measurement configuration, and the scattered field

Let us assume a homogeneous domain $\Omega \subset \mathbb{R}^2$ containing multiple small objects denoted by D_s, with a smooth boundary ∂D_s for $s = 1, 2, \ldots, S$. These objects are modeled as small circular disks centered at $\mathbf{r}_s$ with radius α_s and are presumed to be sufficiently isolated from one another. For a given angular frequency of the operation $\omega = 2\pi f$, the background domain Ω and each object D_s are characterized by their magnetic permeability, i.e., the values of electric conductivity and dielectric permittivity are constant such that $\sigma(\mathbf{r}) \equiv \sigma_0 \approx 0$ and $\varepsilon(\mathbf{r}) \equiv \varepsilon_0 = 8.854 \times 10^{-12}$ F/m. Consequently, by letting μ_s and $\mu_0 = 4\pi \times 10^{-7}$ H/m be the values of the magnetic permeability of D_s and Ω, respectively, the distribution of permeability $\mu(\mathbf{r})$ over the entire domain can be described by the following piecewise constant function:

$$\mu(\mathbf{r}) = \begin{cases} \mu_s, & \mathbf{r} \in D_s, \\ \mu_0, & \mathbf{r} \in \Omega \setminus \overline{D}, \end{cases} \quad \text{where} \quad D = \bigcup_{s=1}^{S} D_s.$$

With this, the background wavenumber is defined as $k_0 = \omega\sqrt{\epsilon_0 \mu_0}$.

Let $\mathbf{a}_m$ ($m = 1, 2, \ldots, M$) and $\mathbf{b}_n$ ($n = 1, 2, \ldots, N$) represent the positions of the transmitter $\mathcal{A}$ and the receivers $\mathcal{B}$, respectively. Using polar coordinates, we set $\mathbf{a}_m$ and $\mathbf{b}_n$ as

$$\mathbf{a}_m = A\boldsymbol{\vartheta}_m = A(\cos\vartheta_m, \sin\vartheta_m) \quad \text{and} \quad \mathbf{b}_n = B\boldsymbol{\theta}_n = B(\cos\theta_n, \sin\theta_n),$$

respectively (see Figure 1), where A and B denote the radii of the transmitter and receiver locations, respectively.

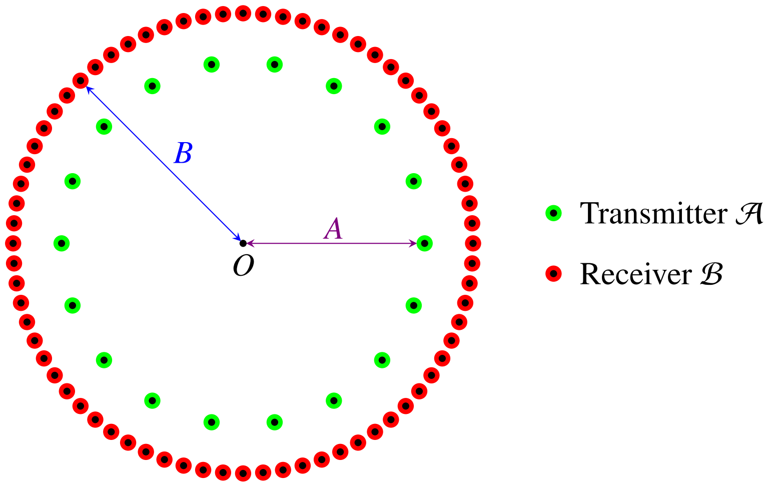

Figure 1. Illustration of transmitter and receiver arrangements.

Throughout this paper, the time-harmonic dependence of $e^{i\omega t}$ is assumed. The incident field generated by a point source at $\mathbf{a}_m$ can be formulated using Green's function: For $\mathbf{r} \in \Omega$,

$$u_{\text{inc}}(\mathbf{r}, \mathbf{a}_m) = G(\mathbf{r}, \mathbf{a}_m) = \frac{i}{4} H_0^{(2)}(k_0|\mathbf{r} - \mathbf{a}_m|), \tag{2.1}$$

where $H_0^{(2)}$ denotes the zeroth-order Hankel function of the second kind. Let $u(\mathbf{r}, \mathbf{a}_m)$ denote the total field at a position $\mathbf{r} \in \Omega$ corresponding to an incident field originating from the transmitting antenna located at $\mathbf{a}_m$. Then, the total field $u(\mathbf{r}, \mathbf{a}_m)$ satisfies the following scalar Helmholtz equation:

$$\nabla \cdot \left(\frac{1}{\mu(\mathbf{r})} \nabla u(\mathbf{r}, \mathbf{a}_m) \right) + \omega^2 \varepsilon_0 u(\mathbf{r}, \mathbf{a}_m) = 0 \quad \text{in} \quad \Omega$$

with the transmission condition

$$\frac{1}{\mu_s} \frac{\partial u(\mathbf{r}, \mathbf{a}_m)}{\partial \boldsymbol{\nu}(\mathbf{r})}\bigg|_{-} - \frac{1}{\mu_0} \frac{\partial u(\mathbf{r}, \mathbf{a}_m)}{\partial \boldsymbol{\nu}(\mathbf{r})}\bigg|_{+} \quad \text{on} \quad \partial D_s, \quad s = 1, 2, \ldots, S,$$

provided the following limit exists:

$$\frac{\partial u(\mathbf{r}, \mathbf{a}_m)}{\partial \boldsymbol{\nu}(\mathbf{r})}\bigg|_{\pm} := \lim_{h \to 0} \nabla u(\mathbf{r} \pm h\boldsymbol{\nu}(\mathbf{r}), \mathbf{a}_m) \cdot \boldsymbol{\nu}(\mathbf{r}),$$

where $\boldsymbol{\nu}(\mathbf{r})$ denotes the unit outward normal vector at position $\mathbf{r}$. Furthermore, the total field measured at the receiving antenna $\mathbf{b}_n$, when the incident field is emitted from $\mathbf{a}_m$, is denoted by $u(\mathbf{b}_n, \mathbf{a}_m)$.

Let us incorporate the measurement data as the scattered field $u_{\mathrm{scat}}(\mathbf{b}_n, \mathbf{a}_m)$, which is defined as the difference between the total and incident fields. Note that it satisfies the following Sommerfeld radiation (or outgoing wave) condition:

$$\lim_{|\mathbf{r}|\to\infty} \sqrt{|\mathbf{r}|}\left(\frac{\partial u_{\mathrm{scat}}(\mathbf{r}, \mathbf{r}')}{\partial|\mathbf{r}|} + ik_0 u_{\mathrm{scat}}(\mathbf{r}, \mathbf{r}')\right) = 0 \quad \text{uniformly in all directions} \quad \frac{\mathbf{r}}{|\mathbf{r}|}.$$

In order to introduce the imaging function, one needs a representation formula for the scattered field data $u_{\mathrm{scat}}(\mathbf{b}_n, \mathbf{a}_m)$. Owing to [2], $u_{\mathrm{scat}}(\mathbf{b}_n, \mathbf{a}_m)$ can be represented by a double-layer potential integral incorporating an unknown density function $\psi(\mathbf{r}, \mathbf{a}_m) \in L^2(\partial D)$:

$$u_{\mathrm{scat}}(\mathbf{b}_n, \mathbf{a}_m) = \int_{\partial D} \frac{\partial G(\mathbf{b}_n, \mathbf{r})}{\partial \boldsymbol{\nu}(\mathbf{r})} \psi(\mathbf{r}, \mathbf{a}_m) d\mathbf{r}. \tag{2.2}$$

However, without prior knowledge regarding the object D, deriving a closed-form expression for the density function ψ is unfeasible. Consequently, to design an imaging function, we adopt the following asymptotic expansion formula derived in [48].

Lemma 2.1. *For a sufficiently high frequency f, the scattered field $u_{\mathrm{scat}}(\mathbf{b}_n, \mathbf{a}_m)$ can be represented as*

$$u_{\mathrm{scat}}(\mathbf{b}_n, \mathbf{a}_m) = 2\pi \sum_{s=1}^{S} \alpha_s^2 \left(\frac{\mu_s - \mu_0}{\mu_s + \mu_0}\right) \nabla G(\mathbf{b}_n, \mathbf{r}_s) \cdot \nabla G(\mathbf{a}_m, \mathbf{r}_s) + o(\alpha_s^2), \tag{2.3}$$

where $o(\alpha_s^2)$ is uniform in $\mathbf{r}_s \in D_s$, $s = 1, 2, \ldots, S$.

Remark 2.1 (Transverse magnetic polarization)**.** *Based on [49], transverse magnetic (TM) polarization represents a scenario where the electric field is aligned parallel to the invariant axis of the scatterer. In this case, for a non-magnetic medium ($\mu(\mathbf{r}) = \mu_0$ for $\mathbf{r} \in \Omega$), the time-harmonic total field $u(\mathbf{r}, \mathbf{a}_m)$ satisfies the following scalar Helmholtz equation:*

$$\triangle u(\mathbf{r}, \mathbf{a}_m) + k_0^2 u(\mathbf{r}, \mathbf{a}_m) = 0 \quad \textit{in} \quad \Omega$$

with the transmission condition

$$u(\mathbf{r}, \mathbf{a}_m)|_- - u(\mathbf{r}, \mathbf{a}_m)|_+ \quad \textit{on} \quad \partial D_s, \quad s = 1, 2, \ldots, S.$$

2.2. Standard BFM-based imaging function

Here, we briefly introduce the standard BFM-based imaging function for identifying D_s. To this end, let us generate a multi-static response (MSR) matrix $\mathbb{K}$ such that

$$\mathbb{K} = \begin{bmatrix} u_{\mathrm{scat}}(\mathbf{b}_1, \mathbf{a}_1) & u_{\mathrm{scat}}(\mathbf{b}_1, \mathbf{a}_2) & \cdots & u_{\mathrm{scat}}(\mathbf{b}_1, \mathbf{a}_M) \\ u_{\mathrm{scat}}(\mathbf{b}_2, \mathbf{a}_1) & u_{\mathrm{scat}}(\mathbf{b}_2, \mathbf{a}_2) & \cdots & u_{\mathrm{scat}}(\mathbf{b}_2, \mathbf{a}_M) \\ \vdots & \vdots & \ddots & \vdots \\ u_{\mathrm{scat}}(\mathbf{b}_N, \mathbf{a}_1) & u_{\mathrm{scat}}(\mathbf{b}_N, \mathbf{a}_2) & \cdots & u_{\mathrm{scat}}(\mathbf{b}_N, \mathbf{a}_M) \end{bmatrix}.$$

Then, by neglecting the asymptotic term $o(\alpha_s^2)$ from (2.3), $\mathbb{K}$ can be written as

$$\mathbb{K} \approx 2\pi \sum_{s=1}^{S} \alpha_s^2 \left(\frac{\mu_s - \mu_0}{\mu_s + \mu_0}\right) \begin{bmatrix} \nabla G(\mathbf{b}_1, \mathbf{r}_s) \cdot \nabla G(\mathbf{a}_1, \mathbf{r}_s) & \cdots & \nabla G(\mathbf{b}_1, \mathbf{r}_s) \cdot \nabla G(\mathbf{a}_M, \mathbf{r}_s) \\ \nabla G(\mathbf{b}_2, \mathbf{r}_s) \cdot \nabla G(\mathbf{a}_1, \mathbf{r}_s) & \cdots & \nabla G(\mathbf{b}_2, \mathbf{r}_s) \cdot \nabla G(\mathbf{a}_M, \mathbf{r}_s) \\ \vdots & \ddots & \vdots \\ \nabla G(\mathbf{b}_N, \mathbf{r}_s) \cdot \nabla G(\mathbf{a}_1, \mathbf{r}_s) & \cdots & \nabla G(\mathbf{b}_N, \mathbf{r}_s) \cdot \nabla G(\mathbf{a}_M, \mathbf{r}_s) \end{bmatrix}$$

$$= 2\pi \sum_{s=1}^{S} r_s^2 \left(\frac{\mu_s - \mu_0}{\mu_s + \mu_0}\right) \begin{bmatrix} \nabla G(\mathbf{b}_1, \mathbf{r}_s)^T \\ \nabla G(\mathbf{b}_2, \mathbf{r}_s)^T \\ \vdots \\ \nabla G(\mathbf{b}_N, \mathbf{r}_s)^T \end{bmatrix} \begin{bmatrix} \nabla G(\mathbf{a}_1, \mathbf{r}_s) & \nabla G(\mathbf{a}_2, \mathbf{r}_s) & \cdots & \nabla G(\mathbf{a}_M, \mathbf{r}_s) \end{bmatrix}.$$

Based on the above, considering conventional BFM-based imaging, the imaging function forms every image point $\mathbf{r} \in \Omega$ through the synthesis inversion of $\nabla G(\mathbf{b}_n, \mathbf{r}) \cdot \nabla G(\mathbf{a}_m, \mathbf{r})$ for all m and n. Correspondingly, the imaging function $\mathfrak{F}(\mathbf{r})$ can be introduced as follows: For each $\mathbf{r} \in \Omega$,

$$\mathfrak{F}(\mathbf{r}) = \left| \sum_{m=1}^{M} \sum_{n=1}^{N} \frac{u_{\text{scat}}(\mathbf{b}_n, \mathbf{a}_m)}{\nabla G(\mathbf{b}_n, \mathbf{r}) \cdot \nabla G(\mathbf{a}_m, \mathbf{r})} \right|. \tag{2.4}$$

Remark 2.2 (Inappropriate imaging function)**.** *Unfortunately, direct application of* (2.4) *is problematic. To explain this, we consider the following:*

$$\nabla G(\mathbf{r}, \mathbf{r}') = -\frac{ik_0(\mathbf{r} - \mathbf{r}')}{4|\mathbf{r} - \mathbf{r}'|} H_1^{(2)}(k_0|\mathbf{r} - \mathbf{r}'|), \quad \textit{for} \quad \mathbf{r} \neq \mathbf{r}'.$$

Then, it is easy to examine that there exists $\mathbf{r} \in \Omega$ *for some* $m, n \in \mathbb{N}$ *such that*

$$\nabla G(\mathbf{b}_n, \mathbf{r}) \cdot \nabla G(\mathbf{a}_m, \mathbf{r}) = -\frac{k_0^2(\mathbf{b}_n - \mathbf{r}) \cdot (\mathbf{a}_m - \mathbf{r})}{16|\mathbf{b}_n - \mathbf{r}||\mathbf{a}_m - \mathbf{r}|} H_1^{(2)}(k_0|\mathbf{b}_n - \mathbf{r}|) H_1^{(2)}(k_0|\mathbf{a}_m - \mathbf{r}|) = 0.$$

This entails the inherent risk that the denominator of the imaging function $\mathfrak{F}(\mathbf{r})$ *of* (2.4) *becomes zero. See Figure 2 for an illustration and Figure 3 for related imaging results.*

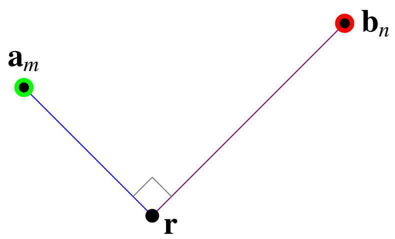

Figure 2. Illustration of the case where $\nabla G(\mathbf{b}_n, \mathbf{r}) \cdot \nabla G(\mathbf{a}_m, \mathbf{r}) = 0$.

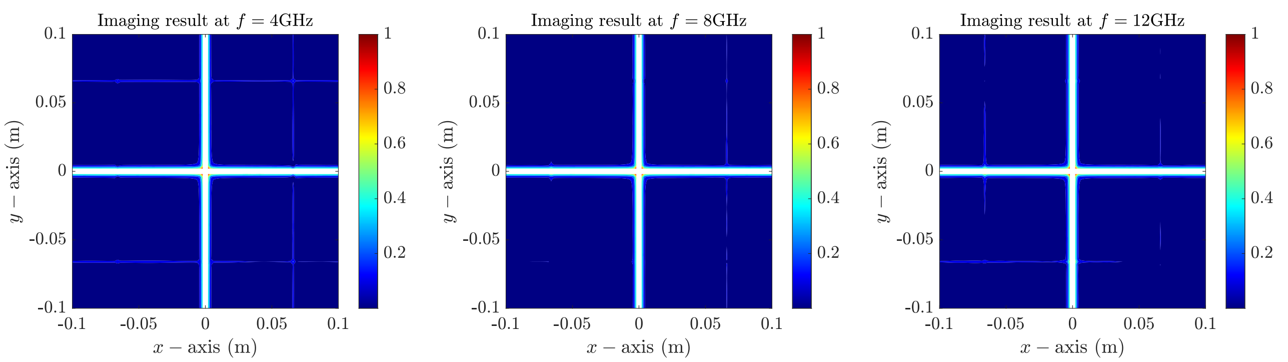

Figure 3. Maps of $\mathfrak{F}(\mathbf{r})$ at $f = 4, 8, 12$ GHz.

Based on Remark 2.2, it seems inappropriate to apply $\mathfrak{F}(\mathbf{r})$ to retrieve D. To avoid these unexpected blow-ups, we adopt a mathematical strategy inspired by [50] and consider the following alternative BFM-based imaging function by replacing the inner product $\nabla G(\mathbf{b}_n, \mathbf{r}) \cdot \nabla G(\mathbf{a}_m, \mathbf{r})$ with $G(\mathbf{b}_n, \mathbf{r})G(\mathbf{a}_m, \mathbf{r})$: For each $\mathbf{r} \in \Omega$,

$$\mathfrak{F}_{\mathrm{BFI}}(\mathbf{r}) = \left| \sum_{m=1}^{M} \sum_{n=1}^{N} \frac{u_{\mathrm{scat}}(\mathbf{b}_n, \mathbf{a}_m)}{G(\mathbf{b}_n, \mathbf{r})G(\mathbf{a}_m, \mathbf{r})} \right|. \tag{2.5}$$

Remark 2.3. *We explicitly note that this denominator substitution is an adopted regularization technique for numerical stability rather than a genuinely new idea of this study. We note that this modification alters the original TE scattering structure, since the leading term for magnetic permeability contrast inherently involves the gradients of Green's functions. However, as demonstrated later in Theorem 3.1 and the numerical simulation results, this modified functional effectively retains the necessary peak properties via Bessel functions. Thus, it remains technically sound and highly appropriate for localizing objects in TE-polarized scattering.*

2.3. Description of the experimental setup and modified BFM-based imaging function

As discussed in Section 2.2, implementing the imaging function in (2.5) requires the acquisition of the complete MSR matrix $\mathbb{K}$. However, practical limitations inherent to the Fresnel experimental setup restrict the receiver's scanning trajectory [47], where the position of the mth transmitter $\mathcal{A}_m$ and nth receiver $\mathcal{B}_n$ are given by

$$\mathbf{a}_m = A\boldsymbol{\vartheta}_m = A(\cos\vartheta_m, \sin\vartheta_m), \quad \vartheta_m = (m-1)\Delta\vartheta = 10^\circ(m-1), \tag{2.6}$$

and

$$\mathbf{b}_n = B\boldsymbol{\theta}_n = B(\cos\theta_n, \sin\theta_n), \quad \theta_n = (n-1)\Delta\theta = 5^\circ(n-1), \tag{2.7}$$

respectively, with $A = 0.720\,\mathrm{m} \pm 0.003\,\mathrm{m}$ and $B = 0.760\,\mathrm{m} \pm 0.003\,\mathrm{m}$. Thus, we set $A = 0.720\,\mathrm{m}$ and $B = 0.760\,\mathrm{m}$. Specifically, for a given transmitter position $\mathbf{a}_m$, the active receiver only covers a partial angular sector defined by $\vartheta_m + 60^\circ \le \theta_n \le \vartheta_m + 300^\circ$ (as illustrated in Figure 4). Consequently, constructing the full MSR matrix is unachievable, rendering the direct application of (2.5) impractical for the reconstruction of the objects D.

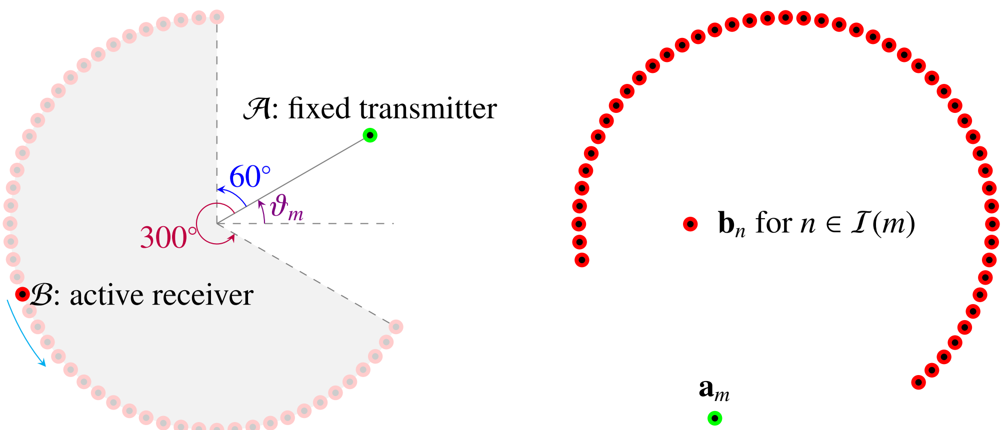

Figure 4. Illustration of receiver rotation corresponding to the transmitter.

To address this incomplete data issue, we partition the receiver indices. Let $\mathcal{I}(m)$ denote the set of indices for active receiver positions $\mathbf{b}_n$ relative to $\mathbf{a}_m$, and let $\mathcal{J}(m)$ represent the complementary set of unmeasured receiver indices. Instead of interpreting the missing data handling as a simple data completion procedure, we explicitly define a binary measurement mask matrix $\mathbb{B} = [b_{nm}]$, where

$$b_{nm} = \begin{cases} 1 & \text{if} \quad n \in \mathcal{I}(m), \\ 0 & \text{if} \quad n \in \mathcal{J}(m). \end{cases} \tag{2.8}$$

We then construct an adapted MSR matrix $\mathbb{A} = [a_{nm}]$ as the Hadamard product of the full MSR matrix $\mathbb{K}$ and the binary measurement mask $\mathbb{B}$ (i.e., $\mathbb{A} = \mathbb{K} \circ \mathbb{B}$), which effectively assigns a value of zero to the unavailable scattered field measurements:

$$a_{nm} = \begin{cases} u_{\text{scat}}(\mathbf{b}_n, \mathbf{a}_m) & \text{if} \quad n \in \mathcal{I}(m), \\ 0 & \text{if} \quad n \in \mathcal{J}(m). \end{cases} \tag{2.9}$$

We refer to Figure 5 for illustrations of the modulus of $\mathbb{A}$, such that $|\mathbb{A}| = [|a_{nm}|]$. It is crucial to clarify the mathematical meaning of these zero entries induced by the binary mask: algebraically, this zero-filling procedure is exactly equivalent to restricting the summation over the receivers from the full set $(n = 1, 2, \ldots, N)$ to the actively measured index set $\mathcal{I}(m)$. By employing this adjusted matrix and the restricted summation, we formulate a modified BFM-based imaging function $\mathfrak{F}_{\text{BFM}}(\mathbf{r})$ as follows: For each $\mathbf{r} \in \Omega$,

$$\mathfrak{F}_{\text{BFM}}(\mathbf{r}) = \frac{|\Phi(\mathbf{r})|}{\max\limits_{\mathbf{r}\in\Omega} |\Phi(\mathbf{r})|}, \quad \text{where} \quad \Phi(\mathbf{r}) = \sum_{m=1}^{M} \sum_{n \in \mathcal{I}(m)} \frac{u_{\text{scat}}(\mathbf{b}_n, \mathbf{a}_m)}{G(\mathbf{b}_n, \mathbf{r}) G(\mathbf{a}_m, \mathbf{r})}. \tag{2.10}$$

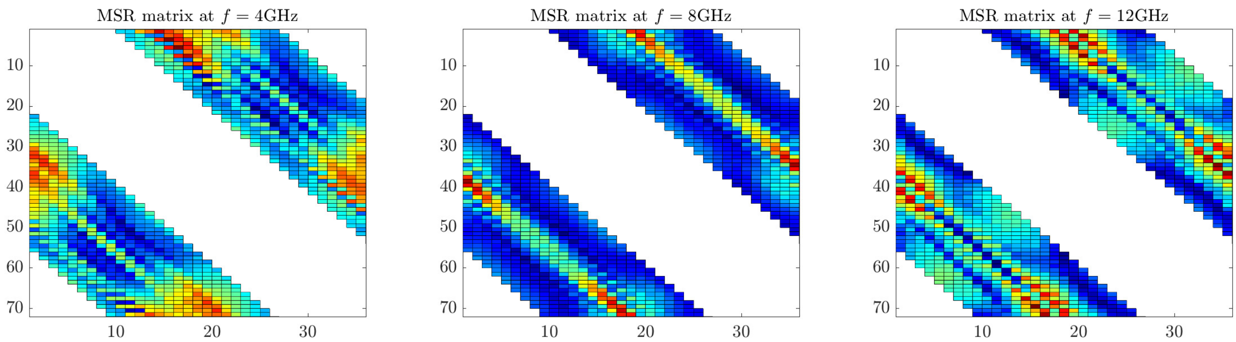

Figure 5. Visualization of $|\mathbb{A}|$ from the dataset `rectTE_8f.exp` in [47].

Remark 2.4. *Note that if one assigns $b_{nm} = C(\neq 0)$ for $n \in \mathcal{J}(m)$ in* (2.8)*, the imaging performance depends significantly on the value of the constant, and it cannot be guaranteed that satisfactory results will be achieved in most scenarios. We refer to [24, 42] for related works.*

3. Structure of the imaging function: Theoretical result and related discussions

Based on the numerical simulation results in Section 4, we can observe that it is possible to recognize the existence and outline shape of D_s through the map of $\mathfrak{F}_{\text{BFM}}(\mathbf{r})$. In order to explain this phenomenon theoretically, we explain that the imaging function can be expressed by an infinite series of the Bessel function of integer order. For a proper derivation, we introduce a useful result derived in [51].

Lemma 3.1 (Representation formula). *Let $\boldsymbol{\theta}_n$ be given by* (2.7)*, $\boldsymbol{\vartheta} \in \mathbb{S}^1 = \{\mathbf{r} \in \mathbb{R}^2 : |\mathbf{r}| = 1\}$, $\mathbf{r} = |\mathbf{r}|(\cos\phi, \sin\phi) \in \mathbb{R}^2$, and $\theta_1 \le \theta \le \theta_N$. Then for sufficiently large N, the following relationship holds uniformly.*

$$\begin{aligned}\frac{1}{N}\sum_{n=1}^{N}(\boldsymbol{\theta}_n\cdot\boldsymbol{\vartheta})e^{ik_0\boldsymbol{\theta}_n\cdot\mathbf{r}} \approx\ & J_0(k_0|\mathbf{r}|)\operatorname{sinc}\frac{\theta_N-\theta_1}{2}\cos\frac{\theta_N+\theta_1-2\vartheta}{2}\\ &+ i\left(\frac{\mathbf{r}}{|\mathbf{r}|}\cdot\boldsymbol{\vartheta}+\operatorname{sinc}(\theta_N-\theta_1)\cos(\theta_N+\theta_1-\vartheta-\phi_s)\right)J_1(k_0|\mathbf{r}|)\\ &+\sum_{p=2}^{\infty} i^p J_p(k_0|\mathbf{r}|)\operatorname{sinc}\frac{(1-p)(\theta_N-\theta_1)}{2}\cos\frac{(1-p)(\theta_N+\theta_1)+2p\phi-2\vartheta}{2}\\ &+\sum_{p=2}^{\infty} i^p J_p(k_0|\mathbf{r}|)\operatorname{sinc}\frac{(1+p)(\theta_N-\theta_1)}{2}\cos\frac{(1+p)(\theta_N+\theta_1)-2p\phi-2\vartheta}{2},\end{aligned} \tag{3.1}$$

where J_p is the Bessel function of order p and sinc *denotes the "sinc function", which is defined as*

$$\operatorname{sinc}(x) = \frac{\sin x}{x}.$$

Specially, if $\theta_N - \theta_1 = 2\pi$, i.e., the full-aperture measurement configuration, then

$$\frac{1}{N}\sum_{n=1}^{N}(\boldsymbol{\theta}_n\cdot\boldsymbol{\vartheta})e^{ik_0\boldsymbol{\theta}_n\cdot\mathbf{r}} \approx i\left(\frac{\mathbf{r}}{|\mathbf{r}|}\cdot\boldsymbol{\vartheta}\right)J_1(k_0|\mathbf{r}|). \tag{3.2}$$

Additionally,

$$\frac{1}{N}\sum_{n=1}^{N} e^{ik_0\boldsymbol{\theta}_n\cdot\mathbf{r}} \approx J_0(k_0|\mathbf{r}|). \tag{3.3}$$

Now, we derive the main result in this paper.

Theorem 3.1 (Asymptotic representation of the imaging function). *Consider the far-field asymptotic regime, where $4k_0|\mathbf{r}-\mathbf{a}_m| \gg 1$ and $4k_0|\mathbf{r}-\mathbf{b}_n| \gg 1$ for all m, n, and $\mathbf{r}\in\Omega$. Furthermore, assume a sufficiently dense angular sampling of transmitters and receivers. Then, by letting $\mathbf{r}_s - \mathbf{r} = |\mathbf{r}_s - \mathbf{r}|(\cos\phi_s, \sin\phi_s)$, the imaging function $\mathfrak{F}_{\mathrm{BFM}}(\mathbf{r})$ can be represented as follows:*

$$\mathfrak{F}_{\mathrm{BFM}}(\mathbf{r}) = \frac{|\Phi(\mathbf{r})|}{\max\limits_{\mathbf{r}\in\Omega}|\Phi(\mathbf{r})|},\quad \Phi(\mathbf{r}) \approx \sum_{s=1}^{S}\alpha_s^2\left(\frac{\mu_s-\mu_0}{\mu_s+\mu_0}\right)\Big(\Lambda(\mathbf{r})+\mathcal{E}(\mathbf{r})\Big), \tag{3.4}$$

where

$$\Lambda(\mathbf{r}) = \left(\operatorname{sinc}\frac{2\pi}{3}\right)J_0(k_0|\mathbf{r}-\mathbf{r}_s|)^2 + \left(1+\operatorname{sinc}\frac{4\pi}{3}\right)J_1(k_0|\mathbf{r}-\mathbf{r}_s|)^2 \tag{3.5}$$

and

$$\mathcal{E}(\mathbf{r}) = \sum_{p=2}^{\infty}\left(\operatorname{sinc}\frac{2(1-p)\pi}{3}+\operatorname{sinc}\frac{2(1+p)\pi}{3}\right)J_p(k_0|\mathbf{r}-\mathbf{r}_s|)^2. \tag{3.6}$$

Proof. Since $4k_0|\mathbf{r}-\mathbf{a}_m| \gg 1$ and $4k_0|\mathbf{r}-\mathbf{b}_n| \gg 1$ for all m, n, and $\mathbf{r} \in \Omega$, the following asymptotic forms hold:

$$\begin{aligned}
H_0^{(2)}(k_0|\mathbf{r}-\mathbf{b}_n|) &= \frac{(1+i)e^{-ik_0B}}{\sqrt{k_0B\pi}} e^{ik_0\boldsymbol{\theta}_n\cdot\mathbf{r}} + O\left(\frac{1}{k_0|\mathbf{r}-\mathbf{b}_n|}\right),\\
H_0^{(2)}(k_0|\mathbf{r}-\mathbf{a}_m|) &= \frac{(1+i)e^{-ik_0A}}{\sqrt{k_0A\pi}} e^{ik_0\boldsymbol{\vartheta}_m\cdot\mathbf{r}} + O\left(\frac{1}{k_0|\mathbf{r}-\mathbf{a}_m|}\right),\\
\nabla H_0^{(2)}(k_0|\mathbf{r}-\mathbf{b}_n|) &= \frac{ik_0(1+i)e^{-ik_0B}}{\sqrt{k_0B\pi}} \boldsymbol{\theta}_n e^{ik_0\boldsymbol{\theta}_n\cdot\mathbf{r}} + O\left(\frac{1}{|\mathbf{r}-\mathbf{b}_n|}\right),\\
\nabla H_0^{(2)}(k_0|\mathbf{r}-\mathbf{a}_m|) &= \frac{ik_0(1+i)e^{-ik_0A}}{\sqrt{k_0A\pi}} \boldsymbol{\vartheta}_m e^{ik_0\boldsymbol{\vartheta}_m\cdot\mathbf{r}} + O\left(\frac{1}{|\mathbf{r}-\mathbf{a}_m|}\right).
\end{aligned}$$

By incorporating truncation error terms of $O((k_0|\mathbf{r}-\mathbf{b}_n|)^{-1})$, $O((k_0|\mathbf{r}-\mathbf{a}_m|)^{-1})$, $O(|\mathbf{r}-\mathbf{b}_n|^{-1})$, and $O(|\mathbf{r}-\mathbf{a}_m|^{-1})$, we can write

$$\frac{\nabla G(\mathbf{b}_n,\mathbf{r}_s)\cdot\nabla G(\mathbf{a}_m,\mathbf{r}_s)}{G(\mathbf{b}_n,\mathbf{r})G(\mathbf{a}_m,\mathbf{r})} \approx -k_0^2(\boldsymbol{\theta}_n\cdot\boldsymbol{\vartheta}_m)e^{ik_0(\boldsymbol{\theta}_n+\boldsymbol{\vartheta}_m)\cdot(\mathbf{r}_s-\mathbf{r})}$$

and correspondingly,

$$\begin{aligned}
\sum_{n\in\mathcal{I}(m)} \frac{\nabla G(\mathbf{b}_n,\mathbf{r}_s)\cdot\nabla G(\mathbf{a}_m,\mathbf{r}_s)}{G(\mathbf{b}_n,\mathbf{r})G(\mathbf{a}_m,\mathbf{r})} &\approx -k_0^2\sum_{n\in\mathcal{I}(m)}(\boldsymbol{\theta}_n\cdot\boldsymbol{\vartheta}_m)e^{ik_0(\boldsymbol{\theta}_n+\boldsymbol{\vartheta}_m)\cdot(\mathbf{r}_s-\mathbf{r})}\\
&= -k_0^2e^{ik_0\boldsymbol{\vartheta}_m\cdot(\mathbf{r}_s-\mathbf{r})}\sum_{n\in\mathcal{I}(m)}(\boldsymbol{\theta}_n\cdot\boldsymbol{\vartheta}_m)e^{ik_0\boldsymbol{\theta}_n\cdot(\mathbf{r}_s-\mathbf{r})}.
\end{aligned}$$

Under the assumption of sufficiently dense angular sampling (M is sufficiently large), the discrete summations over the transmitters can be approximated by continuous angular integrals. This step inherently introduces a discretization error associated with the Riemann sum approximation. Subject to these asymptotic and discretization conditions, since $\theta_1 = \vartheta_m + \pi/3$ and $\theta_N = \vartheta_m + 5\pi/3$, direct application of (3.1) yields

$$\begin{aligned}
&\frac{1}{\#[\mathcal{I}(m)]}\sum_{n\in\mathcal{I}(m)}(\boldsymbol{\theta}_n\cdot\boldsymbol{\vartheta}_m)e^{ik_0\boldsymbol{\theta}_n\cdot(\mathbf{r}_s-\mathbf{r})}\\
&\approx -\left(\operatorname{sinc}\frac{2\pi}{3}\right)J_0(k_0|\mathbf{r}_s-\mathbf{r}|) + i\left(1+\operatorname{sinc}\frac{4\pi}{3}\right)\left(\frac{\mathbf{r}_s-\mathbf{r}}{|\mathbf{r}_s-\mathbf{r}|}\cdot\boldsymbol{\vartheta}_m\right)J_1(k_0|\mathbf{r}_s-\mathbf{r}|)\\
&\quad+\sum_{p=2}^{\infty} i^p(-1)^{p+1}\left(\operatorname{sinc}\frac{2(1-p)\pi}{3}+\operatorname{sinc}\frac{2(1+p)\pi}{3}\right)J_p(k_0|\mathbf{r}_s-\mathbf{r}|)\cos(p(\vartheta_m-\phi_s))
\end{aligned}$$

and correspondingly,

$$\sum_{m=1}^{M}\sum_{n\in\mathcal{I}(m)} \frac{\nabla G(\mathbf{b}_n,\mathbf{r}_s)\cdot\nabla G(\mathbf{a}_m,\mathbf{r}_s)}{G(\mathbf{b}_n,\mathbf{r})G(\mathbf{a}_m,\mathbf{r})} \approx -k_0^2\#[\mathcal{I}(m)]\sum_{m=1}^{M} e^{ik_0\boldsymbol{\vartheta}_m\cdot(\mathbf{r}_s-\mathbf{r})}\Big(\Psi_1+\Psi_2+\Psi_3\Big), \tag{3.7}$$

where $\#[\mathcal{I}(m)]$ denotes the cardinality of the set $\mathcal{I}(m)$, i.e., the total number of actual receiving locations per emission, and

$$\Psi_1 = -\left(\operatorname{sinc}\frac{2\pi}{3}\right)J_0(k_0|\mathbf{r}_s-\mathbf{r}|),$$

$$\Psi_2 = i\left(1+\operatorname{sinc}\frac{4\pi}{3}\right)\left(\frac{\mathbf{r}_s-\mathbf{r}}{|\mathbf{r}_s-\mathbf{r}|}\cdot\boldsymbol{\vartheta}_m\right)J_1(k_0|\mathbf{r}_s-\mathbf{r}|),$$
$$\Psi_3 = \sum_{p=2}^{\infty} i^p(-1)^{p+1}\left(\operatorname{sinc}\frac{2(1-p)\pi}{3}+\operatorname{sinc}\frac{2(1+p)\pi}{3}\right)J_p(k_0|\mathbf{r}_s-\mathbf{r}|)\cos(p(\vartheta_m-\phi_s)).$$

First, direct application of (3.3) yields:

$$\sum_{m=1}^{M} e^{ik_0\boldsymbol{\vartheta}_m\cdot(\mathbf{r}_s-\mathbf{r})}\Psi_1 = -\left(\operatorname{sinc}\frac{2\pi}{3}\right)J_0(k_0|\mathbf{r}_s-\mathbf{r}|)\sum_{m=1}^{M} e^{ik_0\boldsymbol{\vartheta}_m\cdot(\mathbf{r}_s-\mathbf{r})} \approx -M\left(\operatorname{sinc}\frac{2\pi}{3}\right)J_0(k_0|\mathbf{r}_s-\mathbf{r}|)^2. \tag{3.8}$$

Next, by applying (3.2),

$$\begin{aligned}\sum_{m=1}^{M} e^{ik_0\boldsymbol{\vartheta}_m\cdot(\mathbf{r}_s-\mathbf{r})}\Psi_2 &= i\left(1+\operatorname{sinc}\frac{4\pi}{3}\right)J_1(k_0|\mathbf{r}_s-\mathbf{r}|)\sum_{m=1}^{M}\left(\frac{\mathbf{r}_s-\mathbf{r}}{|\mathbf{r}_s-\mathbf{r}|}\cdot\boldsymbol{\vartheta}_m\right)e^{ik_0\boldsymbol{\vartheta}_m\cdot(\mathbf{r}_s-\mathbf{r})}\\ &\approx -M\left(1+\operatorname{sinc}\frac{4\pi}{3}\right)J_1(k_0|\mathbf{r}_s-\mathbf{r}|)^2.\end{aligned} \tag{3.9}$$

Finally, for $p,q,r\in\mathbb{R}$, since $\sin(p\pi-p\alpha)=(-1)^{p+1}\sin(p\alpha)$ and

$$\int_0^{2\pi}\cos(p\vartheta+r)\cos(q\vartheta+r)d\vartheta = \begin{cases}\pi & \text{if} \quad p=q,\\ 0 & \text{if} \quad p\neq q,\end{cases}$$

we can examine that

$$\sum_{m=1}^{M}\cos(p(\vartheta_m-\phi_s)) \approx \frac{M}{2\pi}\int_0^{2\pi}\cos(p(\vartheta-\phi_s))d\vartheta = 0,$$
$$\sum_{m=1}^{M}\cos(p(\vartheta_m-\phi_s))\cos(q(\vartheta_m-\phi_s)) \approx \frac{M}{2\pi}\int_0^{2\pi}\cos(p(\vartheta-\phi_s))\cos(q(\vartheta-\phi_s))d\vartheta = \pi.$$

Since the following Jacobi-Anger expansion formula holds uniformly,

$$e^{ik_0\boldsymbol{\vartheta}_m\cdot(\mathbf{r}_s-\mathbf{r})} = J_0(k_0|\mathbf{r}_s-\mathbf{r}|)+2\sum_{q=1}^{\infty} i^q J_q(k_0|\mathbf{r}_s-\mathbf{r}|)\cos(q(\vartheta_m-\phi_s)),$$

we have

$$\begin{aligned}\sum_{m=1}^{M} e^{ik_0\boldsymbol{\vartheta}_m\cdot(\mathbf{r}_s-\mathbf{r})}\cos(p(\vartheta_m-\phi_s)) \approx &\frac{M}{2\pi}J_0(k_0|\mathbf{r}_s-\mathbf{r}|)\int_0^{2\pi}\cos(p(\vartheta-\phi_s))d\vartheta\\ &+\frac{M}{\pi}\sum_{q=1}^{\infty} i^q J_q(k_0|\mathbf{r}_s-\mathbf{r}|)\int_0^{2\pi}\cos(q(\vartheta-\phi_s))\cos(p(\vartheta-\phi_s))d\vartheta\\ =&Mi^pJ_p(k_0|\mathbf{r}_s-\mathbf{r}|).\end{aligned}$$

Thus,

$$\begin{aligned}
&\sum_{m=1}^{M} e^{ik_0\boldsymbol{\vartheta}_m\cdot(\mathbf{r}_s-\mathbf{r})}\Psi_3\\
&=\sum_{p=2}^{\infty} i^p(-1)^{p+1}\left(\operatorname{sinc}\frac{2(1-p)\pi}{3}+\operatorname{sinc}\frac{2(1+p)\pi}{3}\right)J_p(k_0|\mathbf{r}_s-\mathbf{r}|)\sum_{m=1}^{M} e^{ik_0\boldsymbol{\vartheta}_m\cdot(\mathbf{r}_s-\mathbf{r})}\cos(p(\vartheta_m-\phi_s))\\
&\approx -M\sum_{p=2}^{\infty}\left(\operatorname{sinc}\frac{2(1-p)\pi}{3}+\operatorname{sinc}\frac{2(1+p)\pi}{3}\right)J_p(k_0|\mathbf{r}_s-\mathbf{r}|)^2=-M\mathcal{E}(\mathbf{r}).
\end{aligned}\tag{3.10}$$

Finally, by plugging (3.8)–(3.10) into (3.7), we can obtain

$$\begin{aligned}
&\sum_{m=1}^{M}\sum_{n\in\mathcal{I}(m)}\frac{\nabla G(\mathbf{b}_n,\mathbf{r}_s)\cdot\nabla G(\mathbf{a}_m,\mathbf{r}_s)}{G(\mathbf{b}_n,\mathbf{r})G(\mathbf{a}_m,\mathbf{r})}\\
&\approx k_0^2M\#[\mathcal{I}(m)]\left[\left(\operatorname{sinc}\frac{2\pi}{3}\right)J_0(k_0|\mathbf{r}_s-\mathbf{r}|)^2+\left(1+\operatorname{sinc}\frac{4\pi}{3}\right)J_1(k_0|\mathbf{r}_s-\mathbf{r}|)^2+\mathcal{E}(\mathbf{r})\right]
\end{aligned}$$

and this leads to (3.4). □

Based on Theorem 3.1, we derive the following result.

Corollary 3.1 (A rough upper bound on $|\mathcal{E}(\mathbf{r})|$). *Under the assumptions of Theorem 3.1, $|\mathcal{E}(\mathbf{r})|$ is bounded above by* 0.2067. *Moreover, the value of $|\mathcal{E}(\mathbf{r})|$ decreases as $O((k_0|\mathbf{r}-\mathbf{r}_s|)^4)$ in the immediate vicinity of the object D_s. Furthermore, numerical evaluations suggest its value remains relatively small when evaluated far from the object D_s.*

Proof. Let

$$a_p=\operatorname{sinc}\frac{2(1-p)\pi}{3}+\operatorname{sinc}\frac{2(1+p)\pi}{3}.$$

Then

$$a_p=\begin{cases}\dfrac{3\sqrt{3}}{2\pi(1-9q^2)}, & p=3q,\\[2mm] -\dfrac{3\sqrt{3}}{4\pi(3q+2)}, & p=3q+1,\\[2mm] \dfrac{3\sqrt{3}}{4\pi(3q+1)}, & p=3q+2,\end{cases}\quad\text{which implies}\quad a_p\le a_2=\frac{3\sqrt{3}}{4\pi}.$$

Notice that since $J_0(x)\le 1$, $J_1(x)\le 0.58186$, and (see [52, Formula 9.1.76])

$$J_0(x)^2+2\sum_{p=1}^{\infty}J_p(x)^2=1,$$

we can observe that

$$\sum_{p=2}^{\infty}J_p(k_0|\mathbf{r}-\mathbf{r}_s|)^2=\frac{1}{2}\Big(1-J_0(k_0|\mathbf{r}-\mathbf{r}_s|)^2-2J_1(k_0|\mathbf{r}-\mathbf{r}_s|)^2\Big)\le\frac{1}{2}.$$

Therefore,

$$|\mathcal{E}(\mathbf{r})| = \left|\left(\operatorname{sinc}\frac{2(1-p)\pi}{3} + \operatorname{sinc}\frac{2(1+p)\pi}{3}\right) J_p(k_0|\mathbf{r}-\mathbf{r}_s|)^2\right|$$
$$\leq a_2 \sum_{p=2}^{\infty} J_p(k_0|\mathbf{r}-\mathbf{r}_s|)^2 \leq \frac{3\sqrt{3}}{8\pi} \approx 0.2067.$$

Suppose that $\mathbf{r}$ is situated in the immediate vicinity of $\mathbf{r}_s \in D_s$. Since $k_0|\mathbf{r}-\mathbf{r}_s| \longrightarrow 0$, the following asymptotic form of the Bessel function holds:

$$J_p(k_0|\mathbf{r}-\mathbf{r}_s|) \approx \frac{1}{p!}\left(\frac{k_0|\mathbf{r}-\mathbf{r}_s|}{2}\right)^p. \tag{3.11}$$

Since the series for $\mathcal{E}(\mathbf{r})$ starts at $p = 2$, the leading term is governed by $J_2(k_0|\mathbf{r}-\mathbf{r}_s|)^2$. Consequently, we obtain $\mathcal{E}(\mathbf{r}) = O((k_0|\mathbf{r}-\mathbf{r}_s|)^4)$, which indicates that the value of $\mathcal{E}(\mathbf{r})$ decreases rapidly and becomes negligible as $\mathbf{r} \longrightarrow \mathbf{r}_s$.

In other words, assume that there exists a small number $\delta > 0$ such that $0 < k_0|\mathbf{r}-\mathbf{r}_s| < \delta \ll o(1)$. Then, since $\delta \ll 1$ and $p \geq 2$, we have $\delta^{2p} \leq \delta^2$. With this, based on (3.11), we can examine

$$|\mathcal{E}(\mathbf{r})| \leq \sum_{p=2}^{\infty}\left|\operatorname{sinc}\frac{2(1-p)\pi}{3} + \operatorname{sinc}\frac{2(1+p)\pi}{3}\right| \cdot \frac{1}{(p!)^2} \cdot \frac{\delta^{2p}}{4^p} < \delta^2 \sum_{p=2}^{\infty} \frac{1}{(p^2-1)(p!)^2 4^p} := \delta^2 \sum_{p=2}^{\infty} b_p.$$

Note that since

$$\frac{b_{p+1}}{b_p} = \frac{p^2-1}{(p+1)^2-1} \cdot \frac{(p!)^2}{((p+1)!)^2} \cdot \frac{4^p}{4^{p+1}} = \frac{p-1}{4p(p+1)(p+2)} := r(p),$$

elementary calculus shows that the sequence $\{b_{p+1}/b_p\}$ is strictly decreasing (see Figure 6 for an illustration of $r(x)$). Thus, using

$$b_2 = \frac{1}{192}, \quad \frac{b_3}{b_2} = \frac{1}{96}, \quad \text{and} \quad \frac{b_{p+2}}{b_{p+1}} \leq \frac{b_{p+1}}{b_p} \quad \text{for} \quad p \geq 2,$$

we have

$$|\mathcal{E}(\mathbf{r})| < \delta^2 \sum_{p=2}^{\infty} b_p = \delta^2\left(b_2 + \frac{b_2}{96} + \frac{b_2}{96^2} + \frac{b_2}{96^3} + \cdots\right) = \frac{\delta^2}{190} \ll o(1).$$

Therefore, the value of $\mathcal{E}(\mathbf{r})$ can be disregarded if the search point is close to the object D_s.

Finally, suppose that $\mathbf{r}$ is situated sufficiently far from $\mathbf{r}_s \in D_s$ such that $k_0|\mathbf{r}-\mathbf{r}_s| \gg 0.25$. As shown in Remark 3.1 and Table 1, numerical evaluations confirm that the magnitude of $\mathcal{E}(\mathbf{r})$ remains sufficiently small and does not exceed the theoretical upper bound of 0.2067, ensuring that it does not disrupt the primary imaging phenomena.

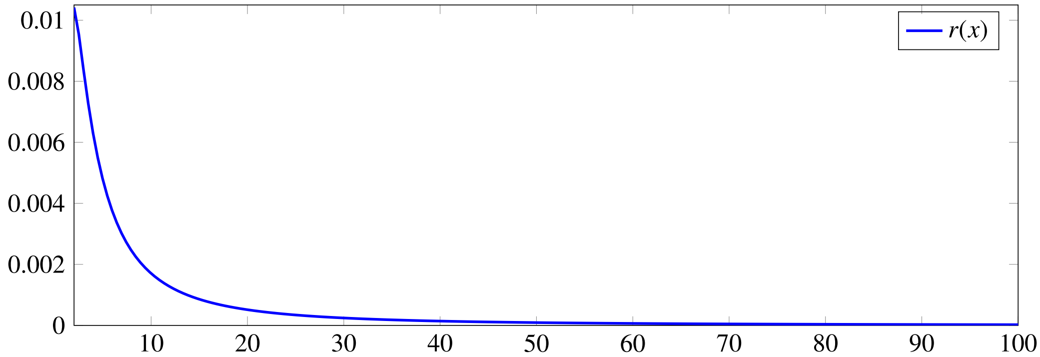

Figure 6. Plot of $r(x)$ for $2 \leq x \leq 100$.

Table 1. Numerical values of max $\mathcal{L}_1(x, P)$ at various frequencies.

	$f = 2\,\text{GHz}$	$f = 4\,\text{GHz}$	$f = 8\,\text{GHz}$	$f = 10\,\text{GHz}$
$P = 10$	4.0583×10^{-3}	4.5404×10^{-3}	4.4791×10^{-3}	3.7562×10^{-3}
$P = 10^2$	1.4641×10^{-4}	1.0609×10^{-4}	1.0076×10^{-4}	1.1261×10^{-4}
$P = 10^3$	0	2.3692×10^{-63}	2.3358×10^{-6}	2.8069×10^{-6}
$P \geq 10^4$	0	0	0	0

□

Remark 3.1 (Numerical validation of Corollary 3.1)**.** *In order to validate the result in Corollary 3.1, we consider the numerical values of* $\mathcal{L}_1(x, P)$*:*

$$\mathcal{L}_1(x, P) = \left| \sum_{s=1}^{2} \sum_{p=2}^{P} \left(\operatorname{sinc} \frac{2(1-p)\pi}{3} + \operatorname{sinc} \frac{2(1+p)\pi}{3} \right) J_p(k_0|x - z_s|)^2 \right| \tag{3.12}$$

with $z_1 = 0.03$ *and* $z_2 = -0.04$*, which serves as the 1D analog of the term* $|\mathcal{E}(\mathbf{r})|$ *from* (3.6)*. As shown in Table 1, the numerical evaluation demonstrates that the maximum value of* $\mathcal{L}_1(x, P)$ *is sufficiently small for* $x \in \mathbb{R}$*. Hence, we can conclude that the term* $|\mathcal{E}(\mathbf{r})|$ *is negligible.*

Based on Theorem 3.1 and Corollary 3.1, we discuss some properties of the imaging function.

Discussion 3.1 (Availability of object detection)**.** *The imaging function consists of the terms* $J_0(k_0|\mathbf{r} - \mathbf{r}_s|)^2$*,* $J_1(k_0|\mathbf{r} - \mathbf{r}_s|)^2$*, and* $\mathcal{E}(\mathbf{r})$*. Since* $J_0(0) = 1$ *and* $J_p(0) = 0$ *for all nonzero integers* p*,* $\mathfrak{F}_{\text{BFM}}(\mathbf{r})$ *is expected to exhibit large-magnitude peaks at* $\mathbf{r} = \mathbf{r}_s \in D_s$*. Furthermore, the properties of* J_0 *introduce an inherent trade-off depending on the applied frequency: While a sufficiently high frequency provides high-resolution imaging, it also generates numerous artifacts. Conversely, operating at a lower frequency reduces these artifacts at the expense of image sharpness. This mathematical structure essentially explains why the modified imaging functional remains perfectly appropriate and effective for TE-polarized scattering despite the absence of the gradient terms in the denominator.*

Discussion 3.2 (Dependence of the frequency of operation)**.** *Building upon Discussion 3.1, we examine the effect of the applied frequency. For a comprehensive analysis, we visualize the following quantity:*

$$\mathcal{L}_2(x) = \left| \sum_{s=1}^{2} \left(\operatorname{sinc} \frac{2\pi}{3} \right) J_0(k_0|x - z_s|)^2 + \sum_{s=1}^{2} \left(1 + \operatorname{sinc} \frac{4\pi}{3} \right) J_1(k_0|x - z_s|)^2 \right|$$

with $z_1 = 0.03$ *and* $z_2 = -0.04$*, which serves as the 1D analog of the term* $\Lambda(\mathbf{r})$ *from* (3.5)*. Figure 7 illustrates that at a sufficiently high frequency (*$f = 8, 10\,\mathrm{GHz}$*),* $\mathcal{L}_2(x)$ *exhibits global maxima exactly at* $x = z_1$ *and* $x = z_2$*, demonstrating that* D_s *can be accurately identified via* $\mathfrak{F}_{\mathrm{BFM}}(\mathbf{r})$*. Conversely, at* $f = 4\,\mathrm{GHz}$*, the global maxima shift to the neighborhood of* z_1 *and* z_2*. While this prevents the exact localization of* D_s*, the presence and total number of the objects remain identifiable at such moderate frequencies. At lower frequencies, however, the global maximum of* $\mathcal{L}_2(x)$ *emerges at* $x = -0.005$*, corresponding to the midpoint of* z_1 *and* z_2*, indicating that low-frequency regimes produce inaccurate imaging results.*

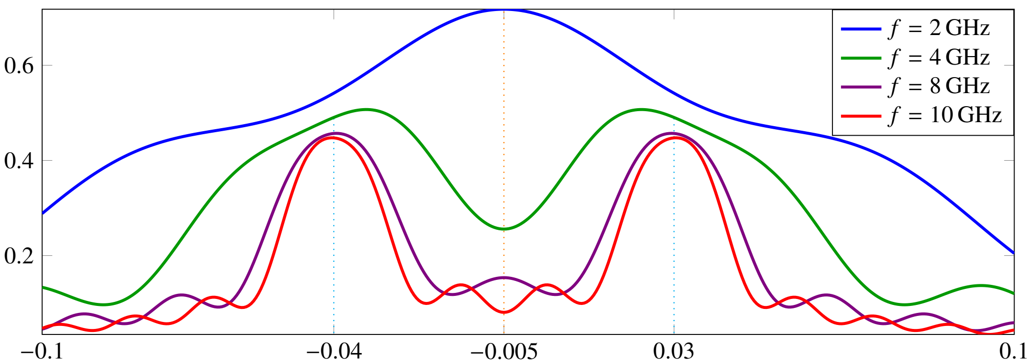

Figure 7. Plots of $\mathcal{L}_2(x)$ at frequencies of $f = 2\,\mathrm{GHz}$, $4\,\mathrm{GHz}$, $8\,\mathrm{GHz}$, and $10\,\mathrm{GHz}$.

Discussion 3.3 (Dependence of material properties)**.** *If* $\mathbf{r} = \mathbf{r}_s \in D_s$ *for* $s = 1, 2, \ldots, S$*, then since*

$$\mathfrak{F}_{\mathrm{BFM}}(\mathbf{r}) \approx \left| \sum_{s=1}^{S} \alpha_s^2 \left(\frac{\mu_s - \mu_0}{\mu_s + \mu_0} \right) \operatorname{sinc} \frac{2\pi}{3} \right|,$$

the value of $\mathfrak{F}_{\mathrm{BFM}}(\mathbf{r})$ *also depends on the size and permeability (i.e., material properties) of* D_s*. For example, if the sizes and permeabilities satisfy*

$$\alpha_1^2 \left(\frac{\mu_1 - \mu_0}{\mu_1 + \mu_0} \right) \ll \alpha_2^2 \left(\frac{\mu_2 - \mu_0}{\mu_2 + \mu_0} \right),$$

then $\mathfrak{F}_{\mathrm{BFM}}(\mathbf{r}_1) \ll \mathfrak{F}_{\mathrm{BFM}}(\mathbf{r}_2)$*. In such a case, the existence and outline shape of* D_2 *can be recognized through the map of* $\mathfrak{F}_{\mathrm{BFM}}(\mathbf{r})$*, while* D_1 *cannot be.*

Discussion 3.4 (Influence of the factor $\mathcal{E}(\mathbf{r})$)**.** *As demonstrated in Corollary 3.1 and Remark 3.1, the magnitude of* $\mathcal{E}(\mathbf{r})$ *is bounded above by* 0.2067 *and decreases as* $O((k_0|\mathbf{r} - \mathbf{r}_s|)^4)$ *in the immediate vicinity of the objects. Although a strict theoretical bound for the far-field is highly complex, numerical evaluations demonstrate that its value remains relatively small. Furthermore, as demonstrated in Discussions 3.1 and 3.2, the principal imaging phenomena, including target* *localization and the frequency-dependent generation of artifacts, are already fully governed by the dominant* $J_0(k_0|\mathbf{r} - \mathbf{r}_s|)^2$ *and* $J_1(k_0|\mathbf{r} - \mathbf{r}_s|)^2$ *terms. Consequently, the influence of* $\mathcal{E}(\mathbf{r})$ *on the map of* $\mathfrak{F}_{\mathrm{BFM}}(\mathbf{r})$ *is extremely minimal. This indicates that the residual infinite series of higher-order Bessel functions comprising* $\mathcal{E}(\mathbf{r})$ *does not significantly interfere with the primary detection peaks, thereby ensuring that the robust identification of the objects remains valid.*

Based on Discussions 3.1–3.4, we can conclude the following result for the qualitative localization of objects.

Corollary 3.2 (Qualitative localization of objects)**.** *Under the same condition as that applied for Theorem 3.1, objects* D_s *can be qualitatively localized through the map of* $\mathfrak{F}_{\mathrm{BFM}}(\mathbf{r})$ *for sufficiently high frequency.*

4. Numerical simulation results: Synthetic and Fresnel experimental dataset

In this section, we present the results of numerical simulations on synthetic and Fresnel experimental datasets to support Theorem 3.1.

4.1. Simulation results with the synthetic dataset

For the synthetic data experiment, we consider three objects D_s ($s = 1, 2, 3$) located at $\mathbf{r}_1 = (0.07\,\mathrm{m}, 0.05\,\mathrm{m})$, $\mathbf{r}_2 = (-0.07\,\mathrm{m}, 0.00\,\mathrm{m})$, and $\mathbf{r}_3 = (0.04\,\mathrm{m}, -0.06\,\mathrm{m})$. Table 2 lists the parameter values of the four experimental cases. The transmitter and receiver setup is identical to that of Subsection 2.3, the homogeneous domain Ω is set to $(-0.1\,\mathrm{m}, 0.1\,\mathrm{m}) \times (-0.1\,\mathrm{m}, 0.1\,\mathrm{m})$, and the maps of $\mathfrak{F}_{\mathrm{BFM}}(\mathbf{r})$ are obtained at frequencies of $f = 2\,\mathrm{GHz}$, $4\,\mathrm{GHz}$, $8\,\mathrm{GHz}$, $10\,\mathrm{GHz}$, and $12\,\mathrm{GHz}$. After generating the unperturbed scattered field data, white Gaussian noise is added to achieve a signal-to-noise ratio (SNR) of 20 dB.

Table 2. Permeabilities and sizes of objects in the synthetic data experiment.

Cases	μ_1	μ_2	μ_3	α_1	α_2	α_3	**References**
Case 1	$5\mu_0$	$5\mu_0$	$5\mu_0$	0.10 m	0.10 m	0.10 m	Example 4.1
Case 2	$3\mu_0$	$5\mu_0$	$7\mu_0$	0.10 m	0.10 m	0.10 m	Example 4.2
Case 3	$5\mu_0$	$5\mu_0$	$5\mu_0$	0.15 m	0.10 m	0.05 m	Example 4.2
Case 4	$3\mu_0$	$5\mu_0$	$7\mu_0$	0.15 m	0.10 m	0.05 m	Example 4.4

Example 4.1 (Objects with the same radii and permeabilities)**.** *Figure 8 illustrates maps of* $\mathfrak{F}_{\mathrm{BFM}}(\mathbf{r})$ *in the presence of* D_s *for Case* 1*. The imaging results indicate that the presence of* D_s *becomes detectable at* $f \geq 4\,\mathrm{GHz}$*. At* $f = 4\,\mathrm{GHz}$*, however, the exact shape of* D_s *cannot be resolved due to blurring, whereas the outlines of all objects* D_s *are clearly identifiable at* $f \geq 6\,\mathrm{GHz}$*. Conversely, at* $f = 2\,\mathrm{GHz}$*, neither the presence nor the shape of all* D_s *can be recognized, whereas at* $f \geq 10\,\mathrm{GHz}$*, the existence and shapes of* D_2 *and* D_3 *can be identified, though recognizing the presence of* D_1 *may remain challenging. Consequently, we conclude that while a sufficiently high frequency enables the determination of both the existence and outline of small objects, low and extremely high frequencies yield poor imaging performance. These findings successfully corroborate Theorem 3.1 as well as Discussions 3.1 and 3.2.*

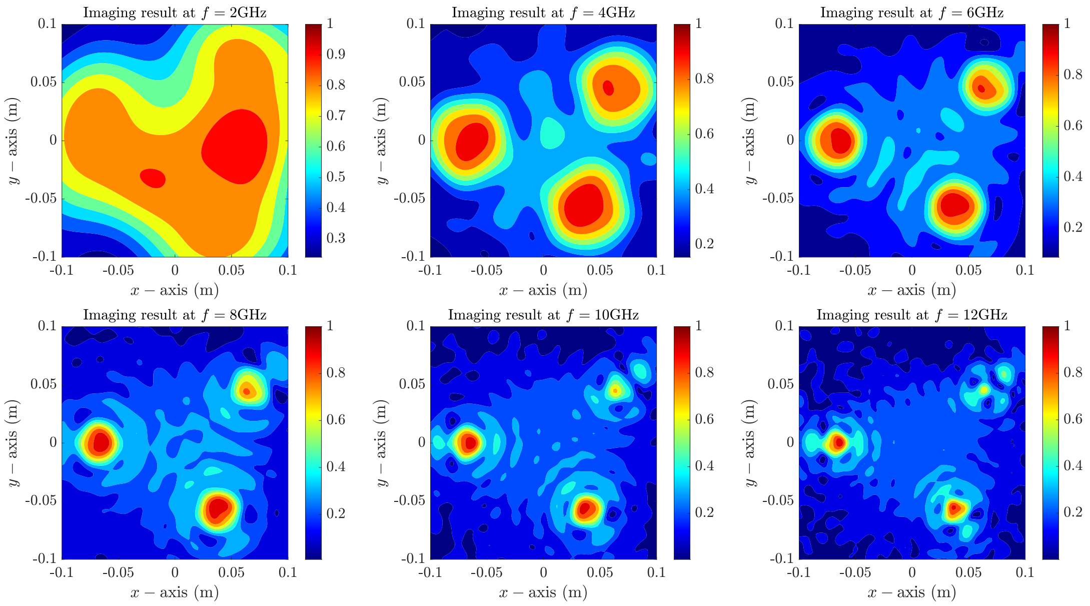

Figure 8. (Example 4.1) Maps of $\mathfrak{F}_{\mathrm{BFM}}(\mathbf{r})$ for Case 1.

Example 4.2 (Objects with different permeabilities)**.** *Figure 9 shows maps of* $\mathfrak{F}_{\mathrm{BFM}}(\mathbf{r})$ *in the presence of* D_s *for Case* 2*. As theoretically predicted in Discussion 3.3, the value of* $\mathfrak{F}_{\mathrm{BFM}}(\mathbf{r})$ *when* $\mathbf{r} \in D_s$ *heavily depends on the material properties of the objects. Consequently, the object* D_3 *with the highest permeability exhibits the most prominent peak, whereas* D_1 *with the lowest permeability appears the weakest. Similar to the observations in Example 4.1, poor imaging performance is observed at a low applied frequency (*$f = 2\,\mathrm{GHz}$*), where the distinct shapes cannot be recognized. At moderate frequencies (*$f = 4\,\mathrm{GHz}$ *to* $8\,\mathrm{GHz}$*), the existence and outlines of the objects are clearly identifiable.*

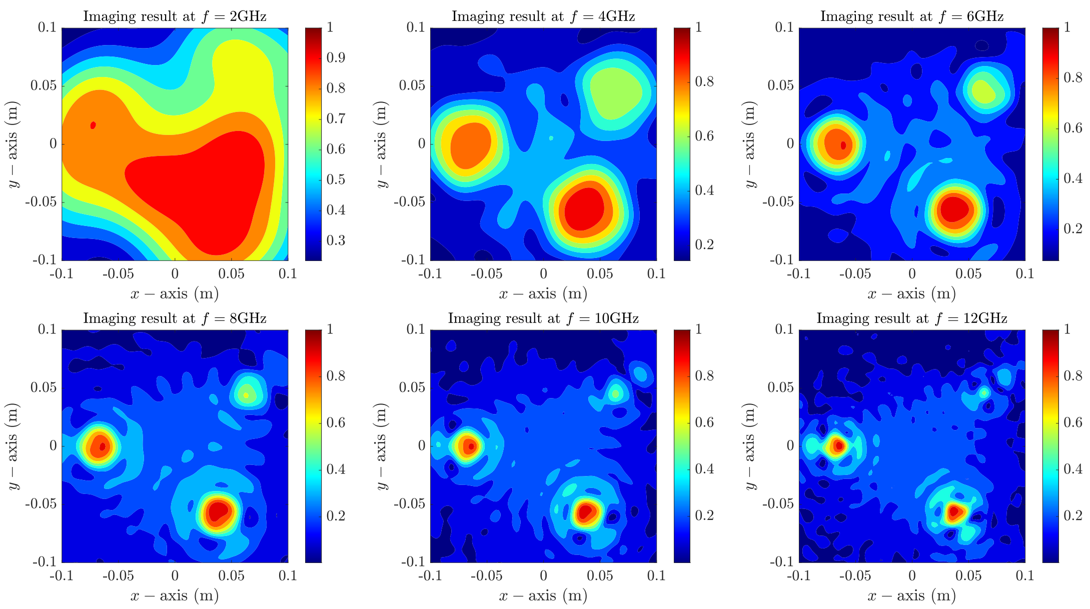

Figure 9. (Example 4.2) Maps of $\mathfrak{F}_{\mathrm{BFM}}(\mathbf{r})$ for Case 2.

Example 4.3 (Objects with different radii)**.** *Figure 10 illustrates the imaging results for Case* 3*. Consistent with the proportional relationship established in Discussion 3.3, the object D_1 with the largest radius dominates the imaging map with the strongest intensity, while the smallest object D_3 is extremely faint and difficult to detect across most frequencies. At extremely high frequencies ($f \geq 10\,\mathrm{GHz}$), artifacts become prominent; the large peak representing D_1 begins to split into multiple artifacts, which makes exact shape reconstruction difficult. Overall, these simulation results successfully confirm that variations in either permeability or size significantly influence the magnitude of the imaging function, thereby corroborating the theoretical expectations outlined in Discussion 3.3.*

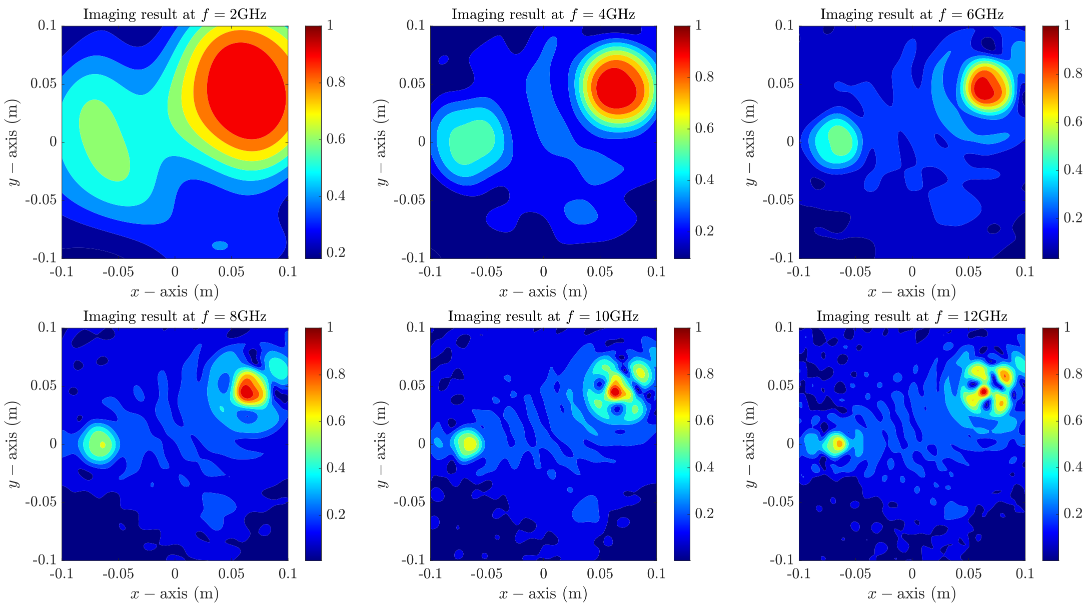

Figure 10. (Example 4.3) Maps of $\mathfrak{F}_{\mathrm{BFM}}(\mathbf{r})$ for Case 3.

Example 4.4 (Objects with different radii and permeabilities)**.** *Here, we consider the identification of small objects where both the radii and permeabilities of the objects vary simultaneously. Figure 11 shows maps of $\mathfrak{F}_{\mathrm{BFM}}(\mathbf{r})$ for Case* 4*. As mentioned in Discussion 3.3, we can observe that the value of $\mathfrak{F}_{\mathrm{BFM}}(\mathbf{r})$ at D_s is proportional to $\alpha_s^2(\mu_s - \mu_0)/(\mu_s + \mu_0)$. At moderate frequencies (e.g., $f = 4\,\mathrm{GHz}$ and $6\,\mathrm{GHz}$), the imaging results are consistent with Discussion 3.3: The dominant peak appears at $\mathbf{r} \in D_1$, whereas D_3 appears extremely faint. At a low frequency ($f = 2\,\mathrm{GHz}$), consistent with the observations in Examples 4.1 and 4.2, the process results in a single blurry artifact dominated by D_1. However, as the frequency increases to $f \geq 8\,\mathrm{GHz}$, the large peak at $\mathbf{r} \in D_1$ splits into multiple severe ring-like artifacts, making its exact shape unidentifiable at $f = 10\,\mathrm{GHz}$ and $12\,\mathrm{GHz}$. Furthermore, D_2 also begins to suffer from similar distortions. Fortunately, we can verify that the value of $\mathfrak{F}_{\mathrm{BFM}}(\mathbf{r})$ reaches a local maximum when $\mathbf{r} \in D_3$ at $f = 10\,\mathrm{GHz}$ and $12\,\mathrm{GHz}$, so identification is possible to some extent. This demonstrates a critical trade-off: while D_1 dominates the imaging map at lower frequencies, higher frequencies are required to properly localize D_2 and D_3, albeit at the cost of distorting the shapes of D_1 and D_2.*

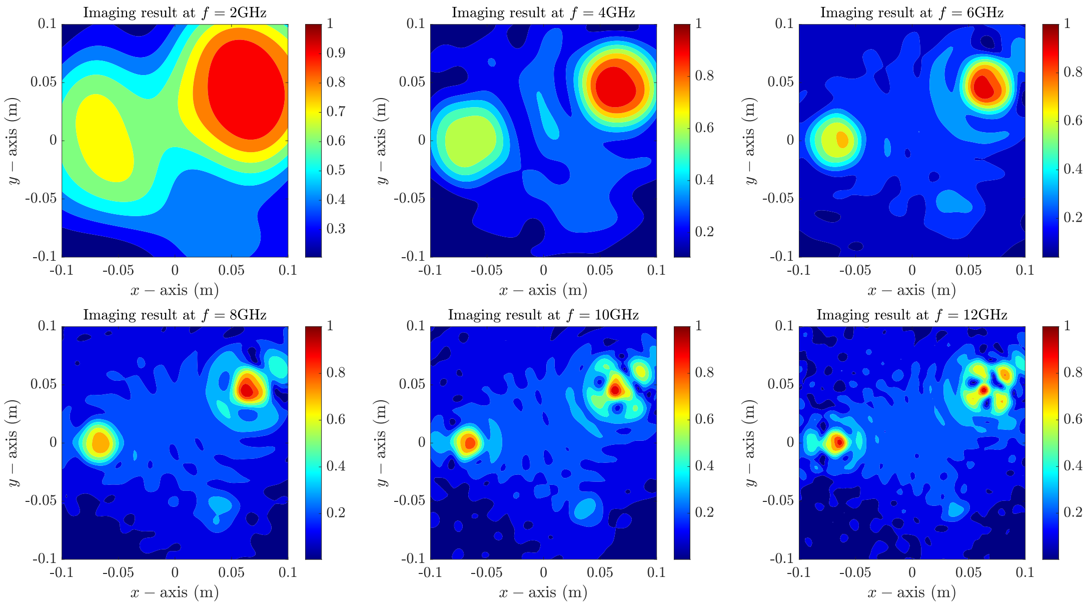

Figure 11. (Example 4.4) Maps of $\mathfrak{F}_{\mathrm{BFM}}(\mathbf{r})$ for Case 4.

Example 4.5 (Imaging with a small number of measurement data)**.** *Here, we consider the effect of the number of measurement data. To this end, we generate an MSR matrix with* $m = 1, 5, \ldots, 33$ *(*$\Delta\vartheta = 40^\circ$ *from* (2.6) *and* $M = 9$*) and* $n = 1, 5, \ldots, 69$ *(*$\Delta\theta = 20^\circ$ *from* (2.7) *and* $N = 18$*), and apply the imaging function* $\mathfrak{F}_{\mathrm{BFM}}(\mathbf{r})$ *for Case* 1*. Based on the imaging results in Figure 12, compared to the results in Example 4.1, the reduced number of transmitters and receivers significantly degrades the overall imaging performance. While the approximate locations of the objects can still be somewhat recognized at moderate frequencies (e.g.,* $f = 4$ GHz*,* 6 GHz*, and* 8 GHz*), the imaging results suffer from severe artifacts and blurring across all frequencies. At lower frequencies (*$f = 2$ GHz*) and extremely high frequencies (*$f = 10$ GHz *and* 12 GHz*), the objects are almost entirely obscured by these artifacts, making it highly difficult to identify their exact existence and outline shapes. These results clearly demonstrate that a sufficient number of measurement data is essential to guarantee accurate localization and shape reconstruction without severe distortion.*

Example 4.6 (Effect of different proportions of missing data)**.** *Here, we examine the influence of the missing data proportions and their configurations on the imaging performance. Figure 13 displays the maps of* $\mathfrak{F}_{\mathrm{BFM}}(\mathbf{r})$ *at* $f = 4$ GHz *for Case* 1 *when the active receiver only covers a partial angular sector defined by* $\vartheta_m + \varphi \le \theta_n \le \vartheta_m + (2\pi - \varphi)$ *corresponding to different active aperture sizes* $\varphi = 120^\circ$, 150°, *and* 180°*. As the proportion of missing data increases, we can observe a significant degradation in both image resolution and amplitude. Notably, the severe lack of multi-static response data introduces a strong directional bias; the identified objects become heavily blurred, and their distinct peaks begin to merge into distorted artifacts. This numerically validates that while zero-filling is a mathematically justifiable strategy within the BFM framework, excessive data omission from severe aperture limitations intrinsically compromises the qualitative localization performance by generating overwhelming artifacts.*

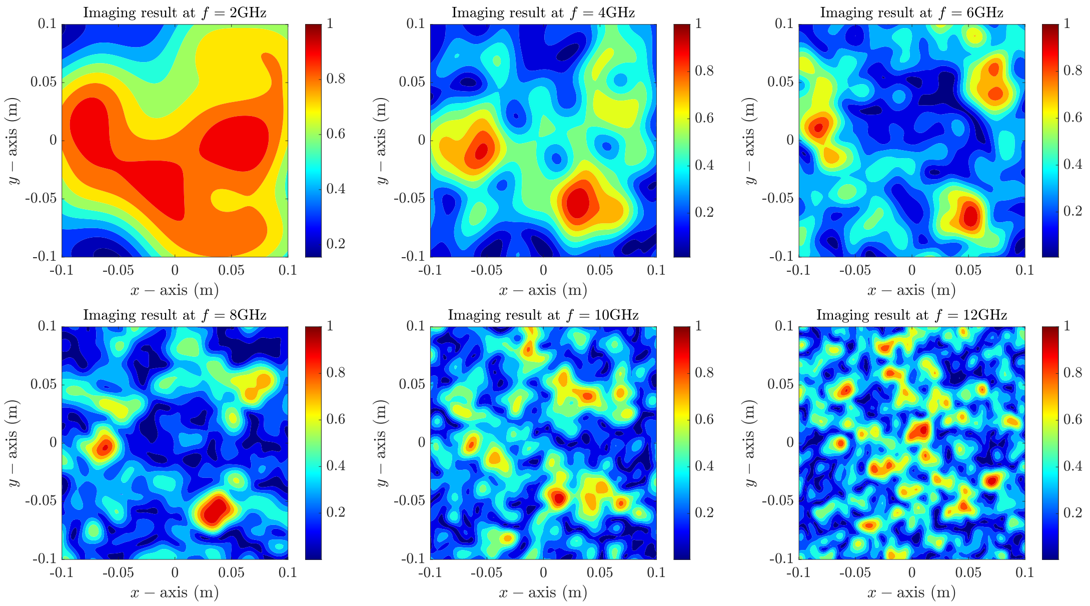

Figure 12. (Example 4.5) Maps of $\mathfrak{F}_{\mathrm{BFM}}(\mathbf{r})$ for Case 1.

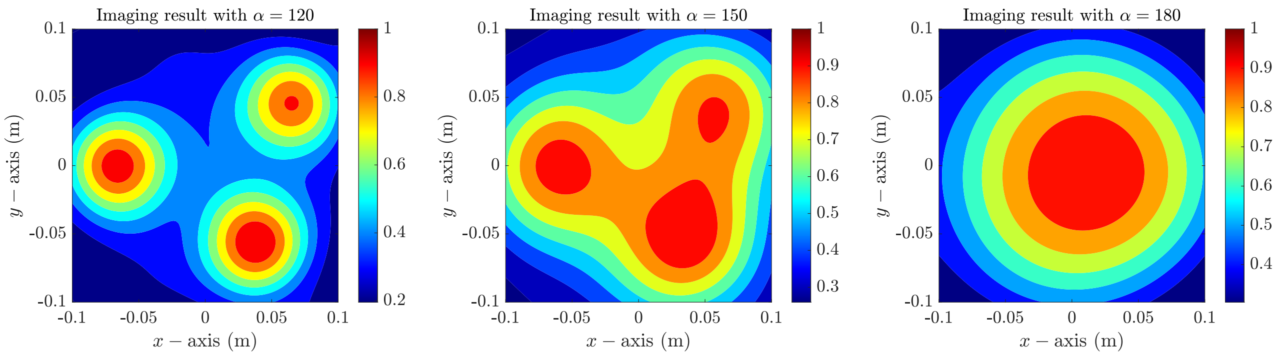

Figure 13. (Example 4.6) Maps of $\mathfrak{F}_{\mathrm{BFM}}(\mathbf{r})$ at $f = 4\,\mathrm{GHz}$ for Case 1.

4.2. Simulation results with the Fresnel experimental dataset

Here, we consider the identification of a perfectly conducting object with a non-smooth boundary using data from the 2D Fresnel experimental dataset `rectTE_8f.exp` (see, e.g., [47]). The simulation setup remains identical to that of the previous examples, except that the object D is a metallic target featuring a rectangular cross-section of dimensions $0.0127\,\mathrm{m} \times 0.0254\,\mathrm{m}$. In contrast to the synthetic data experiments, the numerical simulations were performed without adding artificial noise to the measured scattered field data.

Example 4.7 (Perfectly conducting object with a Lipschitz boundary)**.** *Based on the imaging results exhibited in Figure 14, we can observe that, consistent with the synthetic data simulation results, the location of D cannot be identified at a low applied frequency ($f = 2\,\mathrm{GHz}$). Interestingly, however, in contrast to the synthetic results, two prominent peaks emerge around D. At higher applied frequencies, while the existence and location of D can be recognized, these two large peaks persist. It is interesting* *to note that if a sufficiently high frequency ($f = 10$ GHz and 12 GHz) is applied, it is possible to identify the existence and highly accurate location and shape of D through the map of $\mathfrak{F}_{\mathrm{BFM}}(\mathbf{r})$. Consequently, further research into the identification of metallic objects with a Lipschitz boundary is required to investigate the underlying causes of this phenomenon.*

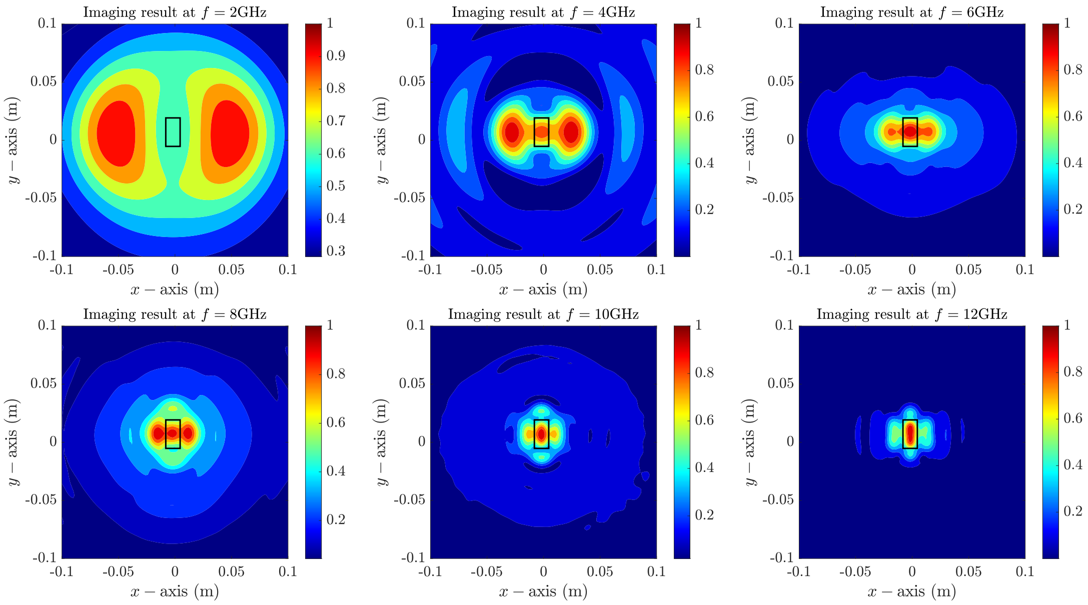

Figure 14. (Example 4.7) Maps of $\mathfrak{F}_{\mathrm{BFM}}(\mathbf{r})$. The black rectangle describes the boundary of the metallic object.

5. Conclusion and perspectives

In this study, we designed and theoretically investigated a modified BFM-based imaging function to localize small penetrable objects using an incomplete MSR matrix obtained from transverse electric polarized waves. Based on the asymptotic expansion formula of the scattered field, we derived an asymptotic representation demonstrating that the imaging function can be expressed as an infinite series comprising Bessel functions of the first kind, the objects' material properties, and the receivers' angular aperture. This theoretical result elucidates why the designed imaging function successfully provides robust qualitative localization by exhibiting high-intensity peaks at the locations of the objects. It also explicitly explains the frequency-dependent nature of the imaging performance: While a sufficiently high frequency provides the necessary resolution to qualitatively localize the presence of the objects, it inevitably introduces multiple artifacts. Conversely, a lower frequency suppresses artifacts at the cost of degraded resolution. Therefore, rather than enabling exact or unique shape recovery, our result confirms that the functional serves as a reliable qualitative indicator. Furthermore, we theoretically predicted and numerically confirmed that the magnitude of the imaging function's output is directly proportional to the permeability and size of the target. Finally, the proposed method successfully provided qualitative localization of the target objects using both synthetic data and a Fresnel experimental dataset for a metallic target with a non-smooth boundary. However, an interesting phenomenon was observed in the experimental results, where two distinct artifact peaks persistently appeared around the target object. To elucidate the fundamental cause of this phenomenon, further in-depth research on the qualitative localization of metallic objects with Lipschitz boundaries is left for future work. Furthermore, extending the current theoretical framework to derive a generalized representation formula with arbitrary aperture-dependent coefficients remains a valuable subject for future research. Furthermore, extending the current theoretical framework to derive a generalized representation formula with arbitrary aperture-dependent coefficients remains a valuable subject for future research.

Author contributions

Taeyoung Ha: Conceptualization, Formal analysis, Funding acquisition, Methodology, Writing–original draft, Writing–review and editing; Sangwoo Kang: Formal analysis, Funding acquisition, Software, Validation, Visualization, Writing–original draft, Writing–review and editing; Minyeob Lee: Formal analysis, Validation, Visualization, Writing–original draft, Writing–review and editing; Won-Kwang Park: Conceptualization, Formal analysis, Funding acquisition, Investigation, Methodology, Validation, Visualization, Writing–original draft, Writing–review and editing; Seong-Ho Son: Funding acquisition, Methodology, Software, Visualization, Writing–original draft, Writing–review and editing. All authors have read and agreed to the published version of the manuscript.

Use of Generative-AI tools declaration

The authors declare they have not used Artificial Intelligence (AI) tools in the creation of this article.

Acknowledgments

This work was supported by the National Research Foundation of Korea (NRF) grant funded by the Korean government (MSIT) (RS-2023-00242528, RS-2025-16067902), in part by the National Institute for Mathematical Sciences (NIMS) Grant funded by the Korean government (NIMS-B26A10000), and by the Soonchunhyang University Research Fund.

Conflict of interest

The authors declare no conflicts of interest regarding the publication of this paper.

References

1. R. C. Aster, B. Borchers, C. H. Thurber, *Parameter Estimation and Inverse Problems*, 2 Eds, Amsterdam: Elsevier, 2013. https://doi.org/10.1016/C2009-0-61134-X
2. D. Colton, R. Kress, *Inverse Acoustic and Electromagnetic Scattering Theory*, 4 Eds, Berlin: Springer, 2019. https://doi.org/10.1007/978-3-030-30351-8
3. N. K. Nikolova, *Introduction to Microwave Imaging*, Cambridge: Cambridge University Press, 2017. https://doi.org/10.1017/9781316084267

4. E. Üregen, A. Yapar, Focusing-based Newton solution for electromagnetic inverse scattering problems, *IEEE Trans. Antennas Propag.*, **72** (2024), 8611–8620. https://doi.org/10.1109/TAP.2024.3460193
5. Y. Qu, H. Dong, An inverse scattering problem for an open sound-hard crack from phaseless data, *Inverse Probl. Imag.*, **23** (2026), 20–50. https://doi.org/10.3934/ipi.2025053
6. H. Muramatsu, S. Kidera, TDOA prior-based contrast source inversion for microwave ablation zone quantitative imaging, *IEEE Trans. Antennas Propag.*, **73** (2025), 3986–3999. https://doi.org/10.1109/TAP.2025.3538218
7. S. H. Kim, L. Pinar, A. H. Hielsher, Accelerated microwave tomographic imaging with a PDE-constrained optimization method, *IEEE Trans. Comput. Imag.*, **11** (2025), 1614–1629. https://doi.org/10.1109/TCI.2025.3629414
8. H. Ammari, P. Garapon, F. Jouve, H. Kang, M. Lim, S. Yu, A new optimal control approach for the reconstruction of extended inclusions, *SIAM J. Control. Optim.*, **51** (2013), 1372–1394. https://doi.org/10.1137/100808952
9. Y. Chang, Y. Guo, D. Zhang, A forward-model-free iterative method for the inverse obstacle scattering problems in three dimensions, *Inverse Probl. Imag.*, **25** (2026), 94–112. https://doi.org/10.3934/ipi.2026017
10. J. K. Seo, E. J. Woo, Magnetic resonance electrical impedance tomography (MREIT), *SIAM Rev.*, **53** (2011), 40–68. https://doi.org/10.1137/080742932
11. V. A. Khoa, G. W. Bidney, M. V. Klibanov, L. H. Nguyen, L. H. Nguyen, A. J. Sullivan, et al., An inverse problem of a simultaneous reconstruction of the dielectric constant and conductivity from experimental backscattering data, *Inverse Probl. Sci. Eng.*, **29** (2021), 712–735. https://doi.org/10.1080/17415977.2020.1802447
12. L. Ballerini, Particle swarm optimization in 3D medical image registration: a systematic review, *Arch. Comput. Meth. Eng.*, **32** (2025), 311–318. https://doi.org/10.1007/s11831-024-10139-x
13. Y. Wang, L. Lin, J. Lv, Numerical method for the inverse scattering problem of acoustic-elastic interaction by random periodic structure, *J. Comput. Phys.*, **562** (2026), 115028. https://doi.org/10.1016/j.jcp.2026.115028
14. O. Kwon, J. K. Seo, J. R. Yoon, A real-time algorithm for the location search of discontinuous conductivities with one measurement, *Commun. Pur. Appl. Math.*, **55** (2002), 1–29. https://doi.org/10.1002/cpa.3009
15. W. K. Park, D. Lesselier, Reconstruction of thin electromagnetic inclusions by a level set method, *Inverse Probl.*, **25** (2009), 085010. https://doi.org/10.1088/0266-5611/25/8/085010
16. K. Ito, B. Jin, J. Zou, A direct sampling method to an inverse medium scattering problem, *Inverse Probl.*, **28** (2012), 025003. https://doi.org/10.1088/0266-5611/28/2/025003
17. S. Kang, M. Lambert, W. K. Park, Direct sampling method for imaging small dielectric inhomogeneities: analysis and improvement, *Inverse Probl.*, **34** (2018), 095005. https://doi.org/10.1088/1361-6420/aacf1d
18. W. K. Park, Direct sampling method for retrieving small perfectly conducting cracks, *J. Comput. Phys.*, **373** (2018), 648–661. https://doi.org/10.1016/j.jcp.2018.07.014

19. A. Kirsch, The factorization method for Maxwell's equations, *Inverse Probl.*, **20** (2004), 117–134. https://doi.org/10.1088/0266-5611/20/6/S08

20. L. Borcea, S. Meng, Factorization method versus migration imaging in a waveguide, *Inverse Probl.*, **35** (2019), 124006. https://doi.org/10.1088/1361-6420/ab2c9b

21. K. H. Leem, J. Liu, G. Pelekanos, An extended direct factorization method for inverse scattering with limited aperture data, *Inverse Probl. Sci. Eng.*, **28** (2020), 754–776. https://doi.org/10.1080/17415977.2019.1647195

22. H. Ammari, J. Garnier, H. Kang, W. K. Park, K. Sølna, Imaging schemes for perfectly conducting cracks, *SIAM J. Appl. Math.*, **71** (2011), 68–91. https://doi.org/10.1137/100800130

23. W. K. Park, Real-time detection of small anomaly from limited-aperture measurements in real-world microwave imaging, *Mech. Syst. Signal Proc.*, **171** (2022), 108937. https://doi.org/10.1016/j.ymssp.2022.108937

24. W. K. Park, On the application of subspace migration from scattering matrix with constant-valued diagonal elements in microwave imaging, *AIMS Math.*, **9** (2024), 21356–21382. https://doi.org/10.3934/math.20241037

25. H. Ammari, E. Iakovleva, D. Lesselier, G. Perrusson, MUSIC type electromagnetic imaging of a collection of small three-dimensional inclusions, *SIAM J. Sci. Comput.*, **29** (2007), 674–709. https://doi.org/10.1137/050640655

26. W. K. Park, Application of MUSIC algorithm in real-world microwave imaging of unknown anomalies from scattering matrix, *Mech. Syst. Signal Proc.*, **153** (2021), 107501. https://doi.org/10.1016/j.ymssp.2020.107501

27. W. K. Park, Application and analysis of MUSIC algorithm for anomaly detection in microwave imaging without a switching device, *Mech. Syst. Signal Proc.*, **243** (2026), 113705. https://doi.org/10.1016/j.ymssp.2025.113705

28. A. Kirsch, S. Ritter, A linear sampling method for inverse scattering from an open arc, *Inverse Probl.*, **16** (2000), 89–105. https://doi.org/10.1088/0266-5611/16/1/308

29. H. F. Alqadah, A compressive multi-frequency linear sampling method for underwater acoustic imaging, *IEEE Trans. Image Process.*, **25** (2016), 2444–2455. https://doi.org/10.1109/TIP.2016.2548243

30. P. Monk, M. Pena, V. Selgas, Multifrequency linear sampling method on experimental datasets, *IEEE Trans. Antennas Propag.*, **71** (2023), 8788–8798. https://doi.org/10.1109/TAP.2023.3298974

31. R. Potthast, A study on orthogonality sampling, *Inverse Probl.*, **26** (2010), 074015. https://doi.org/10.1088/0266-5611/26/7/074015

32. A. Cuccaro, A. Dell'Aversano, M. A. Maisto, G. Leone, R. Solimene, Microwave imaging of small scatterers: linking and comparing the beam-forming and the orthogonality sampling method, *IEEE Trans. Antennas Propag.*, **73** (2025), 3177–3190. https://doi.org/10.1109/TAP.2025.3531661

33. W. K. Park, Inversion of two-dimensional Fresnel experimental dataset using orthogonality sampling method with single and multiple sources: the case of transverse magnetic polarized waves, *Commun. Anal. Mech.*, **18** (2026), 142–171. https://doi.org/10.3934/cam.2026006

34. F. L. Louër, M. L. Rapún, Topological sensitivity for solving inverse multiple scattering problems in 3D electromagnetism. Part I: one step method, *SIAM J. Imag. Sci.*, **10** (2017), 1291–1321. https://doi.org/10.1137/17M1113850

35. A. Carpio, M. Pena, M. L. Rapún, Processing the 2D and 3D Fresnel experimental databases via topological derivative methods, *Inverse Probl.*, **37** (2021), 105012. https://doi.org/10.1088/1361-6420/ac21c8

36. W. K. Park, Performance analysis of multi-frequency topological derivative for reconstructing perfectly conducting cracks, *J. Comput. Phys.*, **335** (2017), 865–884. https://doi.org/10.1016/j.jcp.2017.02.007

37. Y. J. Kim, L. Jofre, F. D. Flaviis, M. Q. Feng, Microwave reflection tomographic array for damage detection of civil structures, *IEEE Trans. Antennas Propag.*, **51** (2003), 3022–3032. https://doi.org/10.1109/TAP.2003.818786

38. L. Jofre, A. Broquetas, J. Romeu, S. Blanch, A. P. Toda, X. Fabregas, et al., UWB tomographic radar imaging of penetrable and impenetrable objects, *Proc. IEEE*, **97** (2009), 451–464. https://doi.org/10.1109/JPROC.2008.2008854

39. L. Jofre, A. P. Toda, J. M. J. Montana, P. C. Carrascosa, J. Romeu, S. Blanch, et al., UWB short-range bifocusing tomographic imaging, *IEEE Trans. Instrum. Meas.*, **57** (2008), 2414–2420. https://doi.org/10.1109/TIM.2008.926382

40. S. Kang, W. K. Park, S. H. Son, A qualitative analysis of bifocusing method for a real-time anomaly detection in microwave imaging, *Comput. Math. Appl.*, **137** (2023), 93–101. https://doi.org/10.1016/j.camwa.2023.02.017

41. S. H. Son, W. K. Park, Application of the bifocusing method in microwave imaging without background information, *J. Korean Soc. Ind. Appl. Math.*, **27** (2023), 109–122. https://doi.org/10.12941/jksiam.2023.27.109

42. S. Kang, M. Lee, W. K. Park, S. H. Son, Application of the bifocusing method in microwave imaging by converting unknown measurement data into the constant, *J. Korean Soc. Ind. Appl. Math.*, **28** (2024), 96–108. https://doi.org/10.12941/jksiam.2024.28.096

43. J. Jeong, S. H. Son, Localization of small moving objects using only total fields in microwave imaging, *Res. Phys.*, **61** (2024), 107777. https://doi.org/10.1016/j.rinp.2024.107777

44. S. Kang, W. K. Park, A novel study on the bifocusing method in two-dimensional inverse scattering problem, *AIMS Math.*, **8** (2023), 27080–27112. https://doi.org/10.3934/math.20231386

45. S. Kang, M. Lee, W. K. Park, S. H. Son, Bifocusing-based imaging of small penetrable dielectric objects from Fresnel dataset, *IEEE Trans. Antennas Propag.*, **73** (2025), 4795–4803. https://doi.org/10.1109/TAP.2025.3550328

46. W. K. Park, On the application of orthogonality sampling method for object detection in microwave imaging, *IEEE Trans. Antennas Propag.*, **71** (2023), 934–946. https://doi.org/10.1109/TAP.2022.3220033

47. K. Belkebir, M. Saillard, Special section: Testing inversion algorithms against experimental data, *Inverse Probl.*, **17** (2001), 1565–1571. https://doi.org/10.1088/0266-5611/21/6/S01

48. H. Ammari, H. Kang, *Reconstruction of Small Inhomogeneities from Boundary Measurements*, Berlin: Springer-Verlag, 2004. https://doi.org/10.1007/b98245

49. T. Rao, X. Chen, Analysis of the time-reversal operator for a single cylinder under two-dimensional settings, *J. Electromagn. Waves Appl.*, **20** (2006), 2153–2165. https://doi.org/10.1163/156939306779322503

50. S. Hou, K. Sølna, H. Zhao, A direct imaging algorithm for extended targets, *Inverse Probl.*, **22** (2006), 1151–1178. https://doi.org/10.1088/0266-5611/22/4/003

51. W. K. Park, Multi-frequency subspace migration for imaging of perfectly conducting, arc-like cracks in full- and limited-view inverse scattering problems, *J. Comput. Phys.*, **283** (2015), 52–80. https://doi.org/10.1016/j.jcp.2014.11.036

52. M. Abramowitz, I. A. Stegun, *Handbook of Mathematical Functions, with Formulas, Graphs, and Mathematical Tables*, New York: Dover, 1996.

AIMS Press